FIRST-PRINCIPLES STUDY OF BINARY GROUP IV-V POLYMORPHS IN 2D TETRAHEX STRUCTURE

A THESIS SUBMITTED TO
THE GRADUATE SCHOOL OF ENGINEERING AND SCIENCE
OF BILKENT UNIVERSITY
IN PARTIAL FULFILLMENT OF THE REQUIREMENTS FOR
THE DEGREE OF
MASTER OF SCIENCE
IN
MATERIALS SCIENCE AND NANOTECHNOLOGY

By
Soheil Ershadrad
August 2021

First-principles study of binary group IV-V polymorphs in 2D tetrahex structure
By Soheil Ershadrad
August 2021

We certify that we have read this thesis and that in our opinion it is fully adequate, in scope and in quality, as a thesis for the degree of Master of Science.

Seymur Jahangirov(Advisor)

Oğuz Gülseren

Ethem Aktürk

Approved for the Graduate School of Engineering and Science:

Ezhan Karaşan
Director of the Graduate School

ABSTRACT

FIRST-PRINCIPLES STUDY OF BINARY GROUP IV-V POLYMORPHS IN 2D TETRAHEX STRUCTURE

Soheil Ershadrad
M.S. in Materials Science and Nanotechnology
Advisor: Dr. Seymur Jahangirov
August 2021

Tetrahex materials are a novel family of 2D materials, made of an ordered sequence of tetragons and hexagons, with exotic electronic, optical and mechanical properties. Motivated by the promising photocatalytic and auxetic properties found in the Tetrahex-carbon, we investigate the behavior of binary group IV-V polymorphs in this structure (denoted by *th*-XY_2 where X = C and Si, and Y = N, P, As, and Sb), through first-principles methods. We demonstrate that these compounds exhibit robust energetic, dynamical, thermal, and mechanical stabilities. Our calculations show that the intrinsic structural anisotropy within this family induces strongly anisotropic mechanical, electronic, and optical behavior. These materials offer high ultimate strain, comparable to that of graphene. The majority are semiconductors in nature, where *th*-CAs_2 and *th*-CP_2 possess direct and quasi-direct band gaps, respectively, and the rest have indirect band gaps. Besides, an indirect-to-direct band gap transition can be induced in *th*-CSb_2 through strain engineering. Studied compounds have good optical absorption in the visible and ultraviolet regions of the light spectrum, suitable for optoelectronics applications. Their band gaps are wide enough to provide the photogenerated energy required for the splitting of water. In *th*-CAs_2 and *th*-CP_2, the positions of band edges are perfectly compatible with the water oxidation and reduction potentials. Besides, they offer anisotropic high charge carrier mobilities, which prolongs the average lifetime of charge carrier drift. Having all these features in one package, these compounds, especially *th*-CAs_2 and *th*-CP_2, can be considered promising candidates for high-performance photocatalytic water splitting. Moreover, we found auxetic behavior in *th*-CN_2 and *th*-SiN_2 around their equilibrium structure. Having this rare feature endows these compounds with potential applicability in numerous areas, from biotechnology to defense.

Keywords: density functional theory, 2D Semiconductor, Photocatalyst, Auxetic.

ÖZET

TETRAHEX YAPSNDAKI GRUP IV-V IKILI POLIMORFLARN ILK ILKELER YÖNTEMI ILE INCELENMESI

Soheil Ershadrad
Malzeme Bilimi ve Nanoteknoloji, Yüksek Lisans
Tez Danışmanı: Dr. Seymur Jahangirov
Augustus 2021

Tetrahex malzemeleri, düzenli bir dörtgen ve altıgen dizisinden oluşan yeni bir iki-boyutlu (2B) malzeme ailesidir ve ilginç elektronik, optik ve mekanik özelliklere sahiptir. Bu çalışmada Tetrahex-karbonda bulunan umut verici fotokatalitik ve auxetic (negatif Poisson oranına sahip) özellikleri göz önünde bulundurarak, bu yapıdaki ikili grup IV V polimorflarının (th-XY_2 ile gösterilir, burada X = C, Si ve Y = N, P, As, Sb) özellikleri yoğunluk fonksiyoneli teorisi kullanarak araştırılmış ve bu bileşiklerin önemli ölçüde enerjik, dinamik, termal ve mekanik kararlılık sergilediği gösterilmiştir. Yaptığımız çalışma bu ailede bulunan yapısal anizotropinin güçlü bir şekilde anizotropik mekanik, elektronik ve optik davranışı tetiklediği göstermektedir. Bu malzemeler, grafen ile karşılaştırılabilecek yüksek nihai gerilme göstermektedir ve çoğunluğu yarı iletkendir. th-CAs_2'de doğrudan bant boşluğu ve th-CP_2'de neredeyse doğrudan bant boşluğu görülmektedir. Ailenin bunlar dışındaki üyeleri dolaylı bant boşluklarına sahiptir. Ayrıca, th-CSb_2'de dolaylı-doğrudan bant aralığı geçişi gerinim mühendisliği ile ulaşılabilir. İncelenen bileşikler görünür ve mor ötesi ışık spektrumunu soğuran özelliğine sahiptir ve optoelektronik uygulamalar için uygundur. Bant aralıkları, suyun ayrışması için gerekli olan fotojenere edilmiş enerjiyi sağlayacak kadar geniştir. th-CAs_2 ve th-CP_2'de bant kenarlarının konumları su oksidasyonu ve redüksiyonu ile mükemmel uyumludur. Ayrıca, yüksek anizotropik yük hareketliliği yük taşınımı ortalama yaşam süresini uzatmaktadır. Tüm bu özellikler sayesinde bu bileşikler, özellikle th-CAs_2 ve th-CP_2, yüksek performanslı fotokatalitik su ayırma için umut verici adaylar olarak kabul edilebilir. Ayrıca, th-CN_2 ve th-SiN_2 bileşiklerinin auxetic davranış sergilediği görülmektedir. Bu nadir özellik, bu bileşiklere biyoteknolojiden savunmaya kadar birçok alanda potansiyel kullanım alanı kazandırabilir.

Anahtar sözcükler: Yoğunluk fonksiyoneli teorisi, iki-boyutlu malzemeler, yarıiletken, fotokataliz, auxetic.

Acknowledgement

I would like to express my deepest gratitude to my supervisor Dr. Seymur Jahangirov for his priceless guidance in academia and in life.

I would like to thank Dr. Oğuz Gülseren and Dr. Ethem Aktürk, who kindly accepted to read, criticize and improve this thesis.

I would like to thank Dr. Salih Demirci for sharing his research experience as a friend and teacher.

I would like to thank Dr. Emin kiliç, who shared his knowledge with me and was a kind mentor for me during my studies.

I would like to thank all my friends in the Institute of Material Science and Nanotechnology.

I would like to thank people of Turkey for their hospitality and kindness.

Finally I would like to thank and dedicate this thesis to my family who have always supported me.

Contents

List of Figures

List of Tables

Chapter 1

Introduction

The advent of graphene [1, 2, 3, 4], in 2004, can be considered as the genesis of the era of 2D materials. In graphene, the presence of two inequivalent Dirac cones at the K and K′ corners of the Brillouin zone (BZ) induces defectless ballistic charge transport, making graphene more conductive than copper [5, 6]. However, the gapless nature of graphene is an obstacle in its functionality in semiconducting and optical absorption applications [7]. Carbon-based 2D compounds, however, can simultaneously offer outstanding electrical and mechanical properties, inherited from their graphene parent, and an energy band gap in the semiconducting region. Thus, in the quest for superior 2D materials, carbon-based compounds gained special popularity. Since carbon offers different hybridization states, including sp, sp^2, and sp^3; not only formation of different carbon-based allotropes are possible but also this feature can be utilized in the design of new carbon-based compounds with different chemical and physical properties [8]. Penta-graphene (PG) [9] and its Stone-Wales defect, tetrahex-carbon (*th*-C) [10], are two recently designed carbon allotropes with sp^2-sp^3 orbital hybridization, which exhibit outstanding electronic, mechanical, and optical properties. PG is the counterpart of graphene with pentagons as its building blocks, offering negative Poisson's ratio and ultrahigh strength [11]. Under the Stone-Wales transformation [12, 13], PG undergoes a structural transition into a more energetically favorable *th*-C phase. The *th*-C shows a direct band gap, high charge carrier mobility, and anisotropic

electronic and optical properties, promising for optoelectronic devices [14, 15]. Although these allotropes of carbon offer some desirable properties in pristine conditions, extra functional features can be induced in them through compounding. Recently, Kilic *et al.* [16] studied the compounds of *th*-C with other group-IV elements, known as *th*-CX (where X = Si, Ge, and alloys). They showed that these compounds are highly stable, satisfying all the requirements needed for synthesizing. *th*-CX compounds offer highly anisotropic mechanical, electronic, and optical properties, and significant potential for photocatalytic water splitting applications. Similarly, upon compounding PG with group-V elements, a metastable family of materials, known as *penta*-CX_2 (where X = N, P, As, and Sb), can be created which offer negative Poisson's ratio, high charge mobilities, and strain-tunable properties, suitable for photocatalysis applications [17, 18, 19]. These are only a few examples, accentuating the promising prospect for the realization of superior and unprecedented properties, through the compounding of 2D carbon allotropes with other chemical elements.

In the family of 2D materials, the out-of-plane quantum confinement provokes special electronic, mechanical, and optical properties, unprecedented in their bulk counterparts [20, 21]. Among these unique features, the extremely high surface-to-volume ratio combined with shorter charge carrier migration distance has made some of the 2D crystals promising for performance enhancement in Hydrogen generation from photocatalytic water splitting [22, 23, 24]. Several studies have indicated that 2D materials can outperform their bulk parents in photocatalysis. For instance, it was shown that photocurrent density produced in 2D SnS_2 [25] and ZnSe [26] crystals are 70 and 200 times greater than their bulk form, respectively. Similar efficiency enhancements were also observed in 2D WS_2 [27] and CdS [28], relative to their bulk forms. Although these results are promising, there is a long road ahead of 2D materials to achieve the desirable photocatalytic efficiency, and superior candidates should be proposed through experimental and theoretical studies.

Materials with a negative Poisson's ratio (PR), known as auxetic, are very rare. In an auxetic crystal, in contrast to a conventional crystal, the thickness increases upon tensile stress and decreases under compressive stress. Among the

few auxetic materials known to this day, the majority have a negative PR only under extreme applied strain. Materials with auxetic behavior around their equilibrium state are even harder to come by [29]. Auxetic materials have promising potential as alignment apparatus and dilator to open up blood vessels in biomedical applications [30], bulletproof armor and vests in defense [31], molecular sieves [32], sensors [33], etc. The appearance of auxetic behavior is reported in both PG and $th-$C structures [9, 16]. However, in $th-$C, negative PR appears only under intensive strain, and not near its equilibrium state. Considering the fact that the configurational prerequisites of auxetic behavior preexist in tetrahex structures, the possibility arises that the compounds formed in this form offer negative PR even in their pristine condition.

Motivated by these possibilities, using first-principles methods, we study *th*-CX_2 (where X = N, P, As, and Sb) and *th*-SiN_2. Tetrahex structures are a novel family of 2D materials, formed by the structural transition from their pentagonal counterparts, upon Stone-Wales transformation. Overall, this thesis is divided into two sections, discussing the properties of *th*-CX_2 (where X = N, P, As, and Sb) compounds in the first part and *th*-XN_2 (where X = C and Si) in the second part. In each section, at first, we discuss the structural properties of the tetrahex compounds, then we investigate their energetic, vibrational, thermal, and mechanical stability. Later, mechanical properties of these materials are investigated, including Young's modulus, Poisson's ratio, and ultimate strain. We show that *th*-XN_2 (where X = C and Si) compounds are among the rare materials that offer auxetic behavior in pristine conditions. Next, electronic band structure and orbitally decomposed projected density of states are discussed. After that, we inspect if these materials have the prerequisites for efficient photocatalytic water splitting. We show that at least two members of this family, namely *th*-CP_2 and *th*-CAs_2 satisfy all the essential requirements for this process, including proper band gap width and band alignment with the redox potential of water splitting, prolonged charge carrier lifetime due to anisotropic carrier mobilities, and suitable solar light absorption coefficient. We also investigate the effect of strain engineering on the electronic and photocatalytic behavior of these materials. Finally, the optical absorption behavior of these compounds is investigated.

Chapter 2

Theoretical Background

In principle, as a quantum mechanical equivalent of Newton's equations of motion, all information about a quantum system can be extracted from the many-body Schrodinger equation [34]:

$$H\Psi_i(r,R) = E_i\Psi_i(r,R) \tag{2.1}$$

where the Hamiltonian is,

$$\hat{H} = -\frac{1}{2}\sum_{i=1}^{N}\nabla_i^2 - \frac{1}{2}\sum_{A=1}^{M}\frac{1}{M_A}\nabla_A^2 - \sum_{i=1}^{N}\sum_{A=1}^{M}\frac{Z_A}{r_{jA}} + \sum_{i=1}^{N}\sum_{j>i}^{N}\frac{1}{r_{ij}} + \sum_{A=1}^{M}\sum_{B>A}^{M}\frac{Z_A Z_B}{R_{AB}} \tag{2.2}$$

Here, the first two terms are related to the kinetic energy of electrons and nuclei, respectively, and the rest are related to the Coulomb interaction among nuclei, electrons, and nuclei-electrons, respectively. However, in realistic cases except for some simple systems such as He or H, this equation is too complicated to offer a calculable solution. To solve this equation, we face 3N + 3M degrees of freedom,

$$\hat{H}\Psi_i(\vec{r_1}, \vec{r_2}, ..., \vec{r_N}, \vec{R_1}, \vec{R_2}, ...\vec{R_M}) = E_i\Psi_i(\vec{r_1}, \vec{r_2}, ..., \vec{r_N}, \vec{R_1}, \vec{R_2}, ...\vec{R_M}) \quad (2.3)$$

where N is the number of electrons and M is the number of nuclei. Therefore, various approximations are employed to simplify this complex equation and through numerical methods, achieve a solution closer to the exact one.

2.1 Born-Oppenheimer Approximation

The first approximation to these kinds of many-body systems is to separate the motion of electrons and nuclei. Considering the fact that the mass of an ion is more than a thousand times higher than the mass of an electron, and consequently, its velocity is at least a thousand times lower, we can assume that electrons will be arranged according to the coordinates of ions before ions positions are changed. This assumption, known as the Born-Oppenheimer approximation, helps to solve the electronic problem, independent of the ionic movements, by assuming a system of fixed ionic coordinates,

$$\hat{H}_{elect} = -\frac{1}{2}\sum_{i=1}^{N}\nabla_i^2 - \sum_{i=1}^{N}\sum_{A=1}^{M}\frac{Z_A}{r_{jA}} + \sum_{i=1}^{N}\sum_{j>i}^{N}\frac{1}{r_{ij}} \quad (2.4)$$

Although promising, this approach leads to an electronic problem that has 3N degrees of freedom and is still hard to solve.

2.2 Hartree-Fock Approximation

Hartree approximation [35] can be employed to simplify the complicated electronic problem. According to this approximation, a many-electron wave function can be written as the product of one-electron wave functions, where each of these

electrons drifts in a potential field which is constructed by the rest of them. Thus, the effect of all electrons can be defined as an effective mean-field one-electron potential ν_i:

$$\sum_{i=1}^{N}\sum_{j>1}^{N}\frac{1}{r_{ij}} \approx \sum_{i=1}^{N}\nu_i(r_i) \tag{2.5}$$

Thus, by employing the Hartree method, after determining an initial effective potential, iterative calculations should be performed until a self-consistent solution is reached that minimizes the total energy. The drawback of this method is that the effect of the Pauli exclusion principle (exchange) is not considered in the approximation. To include the exchange effect, the total wave function can be written as Slater determinants [36], known as the Hartree-Fock method,

$$\Phi_{SD} = \frac{1}{\sqrt{N!}} det\left\{\chi_1(\vec{x_1})\chi_2(\vec{x_2})...\chi_N(\vec{x_N})\right\} \tag{2.6}$$

where, $\frac{1}{\sqrt{N!}}$ is normalization factor, and χ_i are orbital wave function. In this way, 3N degrees of freedom reduce to 3, and numerical calculations will be simplified. Although this approximation considers the exchange effect, the correlation between the many-body electron system is completely neglected [37].

2.3 Density Functional Theory

The first attempts to use the full electron density as the fundamental variable of the electronic many-body problem were done by Thomas and Fermi [38, 39]. Although this approximation failed to include exchange-correlation terms, it created a cornerstone for the rise of Density Functional Theory (DFT).

Hohenberg and Kohn [40], in 1964, introduced the principles of DFT. They proposed that all information regarding the ground state properties of a many-body electronic system is determined by the ground-state electron density. Based on

the first Hohenberg-Kohn theorem, the external potential is a unique functional electron density,

$$E_0\left[\rho_0\right] = \int \rho_0(\vec{r}) V_{ex} d\vec{r} + T\left[\rho_0\right] + E_{ee}\left[\rho_0\right] \tag{2.7}$$

where, ρ_0 is the ground-state electron density, V_{ex} is the external potential, T and E_{ee} are the kinetic and exchange-correlation terms, respectively. According to the second Hohenberg-Kohn theorem, only the true ground state density gives the minimum energy, which paves the path to use the variational principle to find the ground state. In other words, they proved that instead of dealing with the complicated electronic wave functions, the simpler total electron density can be utilized to minimize the total energy of a system,

$$E_0 \leq E\left[\tilde{\rho}\right] = T\left[\tilde{\rho}\right] + E_{ext}\left[\tilde{\rho}\right] + E_{ee}\left[\tilde{\rho}\right] \tag{2.8}$$

Later, in 1965, Kohn and Sham [41] proposed that the kinetic energy of the interacting electrons can be replaced by that of an equivalent non-interacting system to minimize the kinetic energy under predetermined density constraints. After determining the solution to the kinetic term of the equation, the remaining exchange and correlation terms can be also defined as a functional of the full electron density. However, the exact expression is still not derived.

DFT calculations should be performed self-consistently. As it is schematically presented in Fig. 2.1, we start with an initial guess of electron density, for a predefined configuration of ionic coordinates. Then, we calculate the effective potential corresponding to this guessed density. Next, the Kohn-Sham orbitals are calculated by inserting the calculated effective potential into Kohn-Sham equations. From these orbitals, a new electron density is calculated. In the next step, the obtained new electron density gets compared with the initial electron density. Based on Kohn-Sham ansatz, for the ground state, the new and old electron densities should be the same. Thus, if the difference is less than a predefined limit, the required precision is achieved, and the self-consistency loop

will stop. If the difference is more than the acceptable limit, the loop will continue up to a point that the self-consistency is obtained.

2.4 Exchange and Correlation

There are two conventional approximations in order to deal with these two terms. First, the local density approximation (LDA), and second, the generalized gradient approximation (GGA). The main idea behind LDA is to consider the inhomogeneous electronic systems as locally homogeneous ones and then employ the exchange-correlation that corresponds to the homogeneous electron gas for calculations. Thus, LDA gives better approximations in systems with higher degrees of homogeneity. This approximation tends to over bind molecules and solids, but the trends are mostly correct [42]. In the GGA approximation, the inhomogeneities of the density are introduced semi-locally, through expansion of the exchange-correlation functional as a series, including terms of the density and its gradients. In this manner, GGA shows an improvement in binding energies, bond lengths, atomic energies, and bond angles compared to the results obtained from the LDA approximation [43].

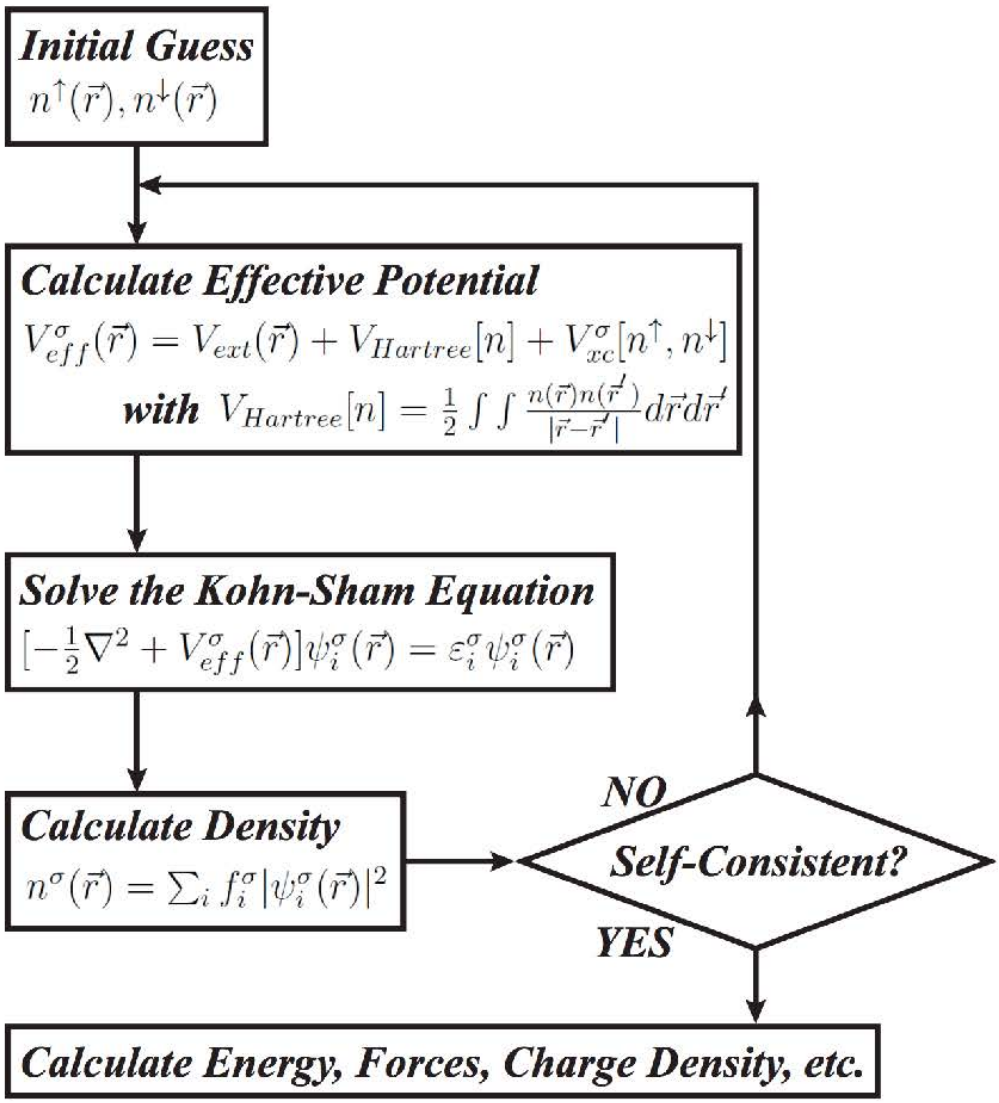

Figure 2.1: The schematic procedure for self-consistent DFT calculations

Chapter 3

Results and discussion

3.1 Methods of calculations

We performed first-principles calculations based on the density functional theory (DFT), using projector-augmented wave potentials [44] and a plane-wave basis set with an energy cutoff of 520 eV. All calculations were performed using the Vienna Ab initio Simulation Package (VASP) [45, 46]. The exchange-correlation potential is approximated by the generalized gradient approximation (GGA) with Perdew, Burke, and Ernzerhof (PBE) functional [47]. For BZ integration, a $18\times18\times1$ k-point grid in the Monkhorst-Pack scheme [48] was used. The equilibrium configuration of atoms, and lattice constants were determined by minimizing the total energy of the system using the conjugate gradient method until force components on each atom were decreased below 0.01 eV/Å. To avoid interaction between periodic images in adjacent cells along the z-axis, a vacuum spacing of at least 20 Å was inserted, and periodic boundary conditions were applied along the x- and y-axis. The energy band gap underestimation, in the PBE scheme, was corrected by the Heyd-Scuseria-Ernzerhof hybrid functional (HSE06), constructed by mixing 25% of nonlocal Fock exchange with 75% of PBE exchange and 100% of PBE correlation energy [49, 50]. To examine the dynamical stability of the structures, phonon dispersion calculations were performed using the Phonopy package [51].

A 4×4×1 supercell with 4×4×1 k-mesh was adopted to calculate the atomic force and the dynamical matrix, with very high accuracy (the convergence criterion of the total energy was set as 10^{-8} eV). To check the thermal stability of the 2D carbides, the *ab-initio* molecular dynamics calculations (AIMD) were performed under constant temperature (T) and volume (V), where the temperature was controlled by a Nose-Hoover thermostat [52, 53, 54]. The total simulation time for the AIMD simulations was taken 20 ps with a time step of 1 fs. For optical response calculations, we employed GW_0 approximation and the Beth-Salpeter equation (BSE) to include electron-hole interactions [55, 56, 57]. Due to the computational limit, k-point sampling was limited to 8×8×1 for the GW_0, and the plane-wave cutoff energy was reduced to 480 eV. The total number of bands was increased to 144 for the GW_0 calculations.

3.2 Tetrahex carbides

3.2.1 Structural properties

The atomic structure of 2D tetrahex carbides with the formula of *th*-XC_2 (X = N, P, As, Sb) is presented in Fig. 3.1. This structure has an orthorhombic unitcell with two unequal lattice constants of a and b, forming a $Cmme$ symmetry (space group no 67). The structure is made of two inequivalent atomic sites, with different coordination numbers, where the 4-fold coordinated positions are occupied by carbon atoms and the 3-fold coordinated locations are filled by the group-V elements, denoted by C and X, respectively. Accordingly, the structure is made of three atomic layers, where a layer made of carbon atoms is sandwiched between two layers of X atoms, and the distance between the top and bottom layer defines the thickness, symbolized by h. To identify the atomic bonds, the bond between C−X and X−X are indicated by d_1 and d_2, respectively. The combination of the tetragonal and hexagonal building blocks in the *th*-XC structure induces peculiar mechanical, electronic, and optical properties, which can be exploited in various applications, especially in photocatalytic water splitting.

The structural properties of *th*-XC_2 compounds are summarized in Table 3.1, and for the sake of comparison, properties of graphene, PG [9], *penta*-XC_2 (X = N, P, As, Sb) [17, 18, 19], *th*-C [10], and *th*-CX (X = Si, Ge) [16] are presented in Table 3.2 As the atomic radius of the group-V elements increases, the lattice constants in both directions expand, in a way that the ratio between them remains almost constant. For the same reason, the bond lengths show a similar increasing trend. For *th*-CN_2, the obtained lattice constants are $a = 4.17$Å and $b = 5.78$ Å, and the layer thickness is found to be 1.48 Å. The calculated bond length of C−N ($d_1 = 1.42$ Å) is compatible with that of *penta*-CN_2 ($d_1 = 1.47$ Å), and the N−N bond length was found to be $d_2 = 1.47$ Å, which is exactly the average bond length of single-bonded N−N, and explicitly shows the single bond nature of N−N dimer. In the case of *th*-CP_2, the elongation in the structure expands the lattice constants into $a = 5.31$ Å, $b = 7.20$ Å, and $h = 2.32$ Å. The C−P bond length ($d_1 = 1.88$ Å) is exactly the same as its counterpart in *penta*-CP_2 (1.88 Å). For *th*-CAs_2, the elongation continues with $a = 5.60$ Å, $b = 8.00$ Å, and $h = 2.52$ Å. Similarly, the bond length of C−As ($d_1 = 2.02$ Å) is precisely equal to its counterpart in *penta*-CAs_2. The same rules apply to *th*-CSb_2 with $a = 6.10$ Å, $b = 9.10$ Å, and $h = 2.81$ Å, where C−Sb bond length ($d_1 = 2.22$ Å) is compatible with C−Sb bond length ($d_1 = 2.21$ Å) in *penta*-CSb_2. In group-V of the periodic table, electrons of *d*-orbital in As and Sb have a weak shielding effect, and cannot cancel out the nucleus attraction force (resulted by their corresponding protons) on the electron cloud effectively. Therefore, the increase in the atomic radius is not linear along the group, and the jump in the bond length between C−N and C−P is more notable compared to C−P and C−As, or C−As and C−Sb. This phenomenon affects the inter-bonding angles too. Thus, although all of the members of *th*-CX_2 family have an overall similar structure, the angles of *th*-CN_2 show a deviation from the rest (*th*-CP_2, *th*-CAs_2, and *th*-CSb_2 have very close bonding angles). In the *th*-CX_2 structures, the thickness is equal to the two times the projection of C−X bonds along the out-of-plane axis. Accordingly, the thickness also increases as we go down in the group, with a notable jump between *th*-CP_2 and *th*-CN_2. These structural properties show that carbon atoms exhibit an sp^3 orbital hybridization, and participate in four σ bonds with surrounding X atoms. To verify this claim, the electron localization function (ELF) plots of the *th*-CX_2

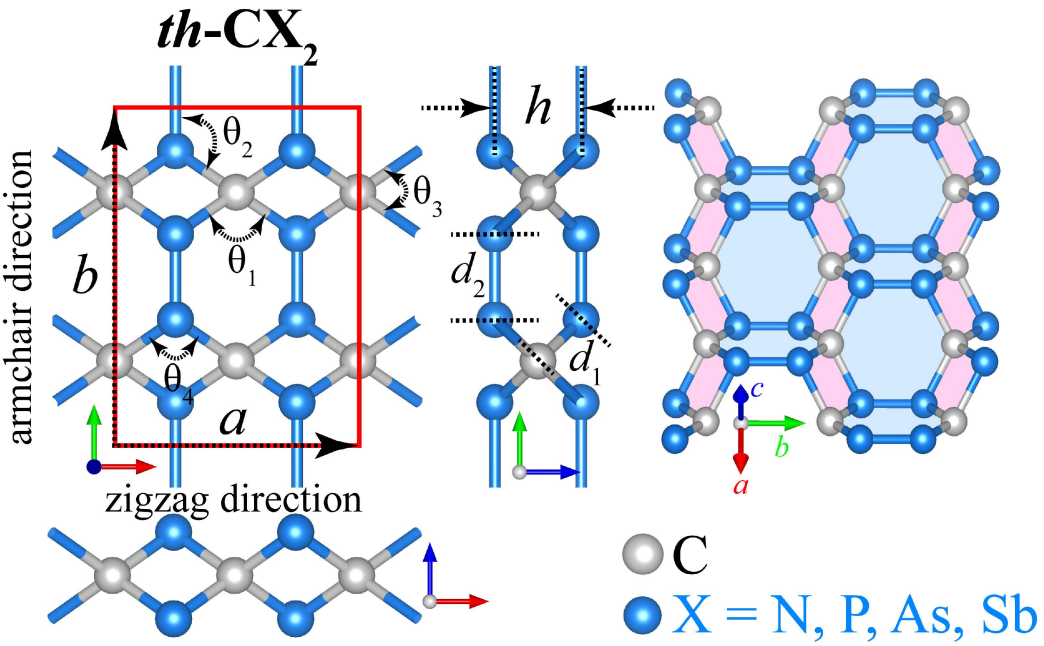

Figure 3.1: Optimized atomic structure of *th*-CX_2 (X = N, P, As, and Sb) from the top and side views. The unit cell is depicted in red line. Blue and gray balls represent X and C atoms, respectively.

compounds are provided in Fig. 3.2. It can be seen that the charge distribution along the bonds is localized in the center, which confirms that all bonds are σ type. Based on the electronegativity difference between carbon and group-V elements, the bonds have covalent nature. In *th*-CP_2, *th*-CAs_2, and *th*-Sb_2, the electronegativity of carbon outweighs that of X atom, consequently, the X−X bonds are slightly longer than their average value for a single bond. In the case of *th*-CN_2, however, the ratio is reversed, and higher electronegativity of nitrogen atoms provides enough charge density to create an N−N bond exactly equal to the length of the average singly bonded N−N dimer ($d = 1.47$ Å).

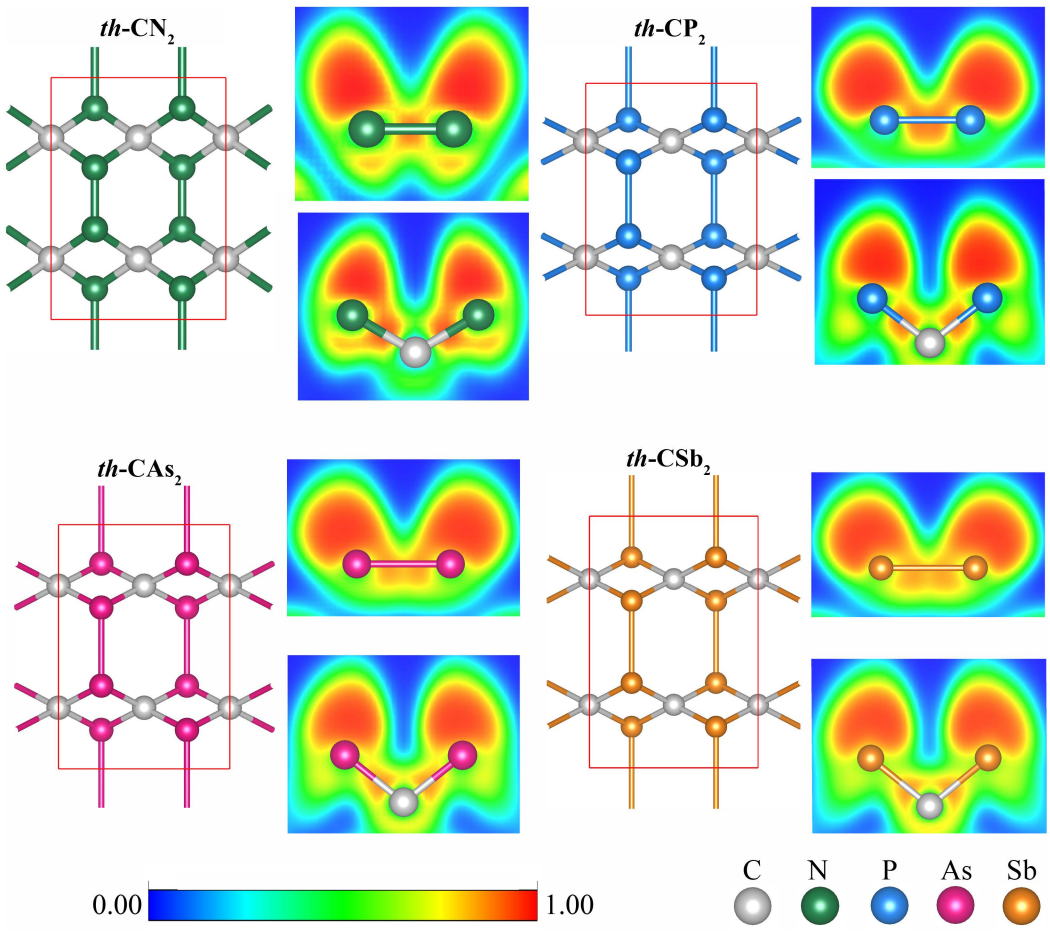

Figure 3.2: The electron localization function (ELF) plots of *th*-CX_2 compounds, indicating the sigma nature of C−X and X−X bonds.

3.2.2 Stability

3.2.2.1 Energetic stability

To examine the synthesizability of the 2D *th*-CX_2 compounds, at the first step, we evaluate their relative cohesive energies (E_{coh}) compared to similar structures that have already been shown to be stable. Cohesive energy is the amount of energy, required to be supplied into a crystal to break the bonds and decompose the structure into its constitutional elements. Cohesive energy can be extracted from the following expression;

Table 3.1: The structural, energetic and electronic properties of the *th*-CX_2 compounds, where a and b are lattice parameters, h is the thickness, $d_{(1-2)}$ are bond lengths in unit of Å, $\theta_{(1-4)}$ are inter-bond angles, E_{coh} is the cohesive energy in unit of eV/atom, E_g^{PBE} and E_g^{HSE} are the band gap energies in unit of eV obtained based on PBE and HSE06 methods, respectively, VBM and CBM are valence band maximum and conduction band minimum in unit of eV calculated using HSE06 functional.

Structure	a	b	h	d_1	d_2	θ_1	θ_2	θ_3	θ_4	E_{coh}	E_g^{PBE}	E_g^{HSE}	VBM	CBM
th-CN_2	4.17	5.78	1.48	1.46	1.46	122	119	89	91	5.19	3.05	4.57	-6.49	-1.92
th-CP_2	5.31	7.20	2.32	1.88	2.28	139	110	90	90	4.61	1.26	2.12	-6.00	-3.88
th-CAs_2	5.60	8.00	2.52	2.02	2.55	138	111	92	88	4.56	1.52	2.31	-5.82	-3.51
th-CSb_2	6.10	9.10	2.81	2.22	2.96	138	111	93	87	3.76	0.60	1.15	-5.05	-3.90

$$E_{coh} = \frac{4E_C + 8E_X - E_T}{12} \tag{3.1}$$

where E_{C} and E_{X} are the energy of carbon and group-V element, respectively, and E_{T} is the total energy of one unitcell of the crystalline structure. It can be inferred that a high enough E_{coh} implies the relative energetic stability of the system. The cohesive energies of 2D *th*-CX_2 compounds are listed in Table 3.1. It can be seen that *th*-CN_2 with $E_{\text{coh}} = 5.19$ eV/atom has the highest cohesive energy among this group, and as the atomic number increases, E_{coh} values decline. This decreasing manner is directly related to the energy of the C−X bonds which are dominant in numbers (12 to 4) within a unitcell. For instance, although the P−P bonds have higher energy compared to N−N bonds (0.35 eV/atom difference in favor of P−P), the 0.42 eV/atom difference in bond energies of C−N and C−P (with 3.16 and 2.55 eV/atom, respectively) is responsible for the 0.58 eV/atom increase in the cohesive energy of *th*-CN_2 compared to *th*-CP_2 [58]. By comparing the cohesive energies of 2D *th*-CX_2 compounds with that of graphene (7.94 eV/atom) [1], *th*-C (7.12 eV/atom) [10], PG (7.09 eV/atom) [9], and *penta*-CN_2 (5.51 eV/atom) [17], we can see that *th*-CX_2 structures have less favorable cohesive energies. However, the cohesive energies of *th*-CX_2 surpass that of already synthesized silicene (4.70 eV/atom) [59], germanene (4.15 eV/atom) [60], and phosphorene (3.48 eV/atom) [61]. Although the cohesive energy cannot directly verify the stability of crystals, the fact that *th*-CX_2 cohesive energy values lie in the range of synthesized structures is a sign that *th*-CX_2 structures are strongly bonded and are synthesizable.

Table 3.2: The structural, energetic and electronic properties of structures comparable to *th*-CX_2, where a and b are lattice parameters, h is the thickness, $d_{(1-2)}$ are bond lengths in unit of Å, E_g is the band gap energy in unit of eV, and Y is the Young's modulus in unit of N/m (references are introduced in the text).

Structure	a	b	h	d_1	d_2	E_g	Gap type	Y
Graphene	2.46	2.46	0.00	1.42	1.42	0.00	-	340
Penta-Graphene	3.64	3.64	1.20	1.34	1.54	6.53	indirect	264
Penta-CN_2	3.31	3.31	1.52	1.47	1.47	6.53	indirect	315
Penta-CP_2	4.09	4.09	-	1.88	1.88	2.64	indirect	60
Penta-CAs_2	4.36	3.36	-	2.02	2.02	2.09	indirect	37
Penta-CSb_2	4.79	4.79	-	2.21	2.21	1.35	indirect	9
Tetrahex-C	4.53	6.10	1.16	1.34	1.53	2.64	direct	286
Tetrahex-SiC	5.53	7.63	1.60	1.71	1.88	1.78	indirect	143
Tetrahex-GeC	5.89	8.07	1.60	1.82	1.98	1.34	indirect	119

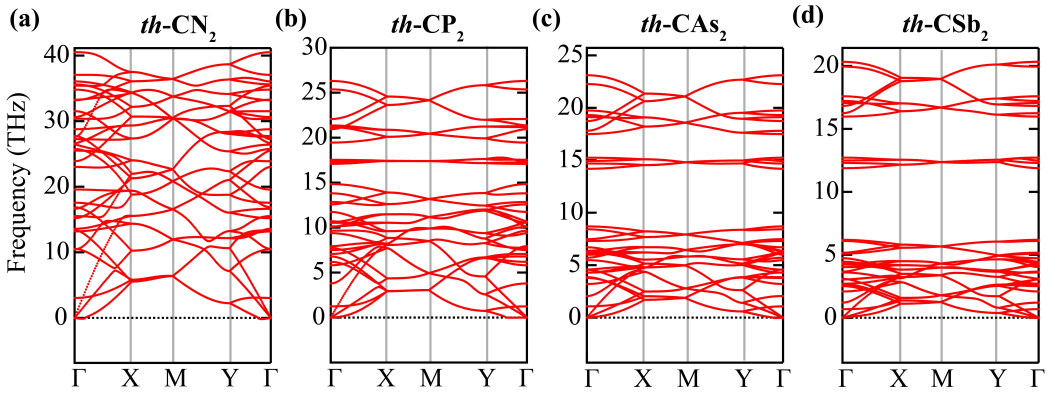

Figure 3.3: The phonon spectrum of the *th*-CX_2 compounds, where the vibrational frequencies in the unit of THz are depicted *vs* the wavenumber (k) along the high symmetry lines of the BZ.

We further calculated the formation energy of the *th*-CX_2 compounds. We found the formation energy of these compounds to be 870, 100, 140, and 190 meV/atom for X = N, P, As, and Sb, respectively. These positive values of formation energy show that the *th*-CX_2 are metastable phases of CX compounds. However, similar to many metastable CX structures that have already been synthesized such as *graphitic*-C_3N_4, the *th*-CX_2 compounds have the energetic stability to be synthesized in the lab.

3.2.2.2 Dynamic stability and phonon properties

In the second step, the dynamic stability of the *th*-CX_2 monolayers were studied based on their phonon dispersions, calculated via *ab-initio* lattice dynamics.

The dispersions of phonon modes are depicted in Fig. 3.3 (a-d). The 12 atoms presented in a unitcell of *th*-CX_2, each has 3 vibrational degrees of freedom, constituting a total of 36 phonon modes, of which 3 are acoustic branches with zero-frequency at Γ point. In all 2D materials, the transverse acoustic (TA) and longitudinal acoustic (LA) branches exhibit a linear dispersion around the Γ point, while the out-of-plane acoustic (ZA) branch has a quadratic dispersion when the wave number approaches zero near the Γ point. Based on the harmonic approximation, since imaginary vibrational frequencies manifest a disassembling harmonic force between atoms, the prerequisite of vibrational stability is that all phonon modes must have real (positive) frequencies. The marginal imaginary frequencies that can be found in the phonon spectrum of the *th*-CX_2 structures around the Γ point stem from the numerical errors in the calculation of force constants, which can be neglected. Thus, the lack of any disassembling force between atoms of the *th*-CX_2 structures guarantees their dynamical stability.

3.2.2.3 Thermal stability

To verify the thermal stability of the *th*-CX_2 compounds, *ab-initio* molecular dynamics simulations (AIMD) were performed at the high temperature for a duration of 20 ps. To reduce the periodic boundary condition constraints on the structure and provide a suitable condition for any possible reconstruction, a relatively large supercell of 4×3×1 times the original unitcell was employed. Snapshots of the final atomic configuration of the structures after 20 ps and the diagrams of potential energy variation *vs* time are provided in Fig. 3.4. We found that *th*-CN_2 and *th*-CP_2 lose their structural integrity at $T = 1400$ K, and textitth-CAs_2 and *th*-CSb_2 become fragmented at $T = 1200$ K. Thus, in our simulation, we considered $T = 1200$ K for *th*-CN_2 and *th*-CP_2, and $T = 1000$ K for *th*-CAs_2 and *th*-CSb_2. It can be seen that the potential energies only fluctuate during the simulation without any considerable deviation, which implies that no reconstruction takes place. These fluctuations are the result of the thermal oscillations of the atoms around their equilibrium positions. From the snapshots of the ultimate arrangement of the atoms, it can be inferred that none of the bonds

Table 3.3: The mechanical properties of the *th*-CX_2 structures, where C_{ij} are the elastic constants in the unit of N/m, Y_x and Y_y are Young's modulus in zigzag and armchair directions in the unit of N/m, ν_x and ν_y are the Poisson's ratios along zigzag and armchair directions, US_x, $_y$, $_{xy}$ are the ultimate strain in % under zigzag, armchair and equi-biaxial strain, respectively.

	Mechanical Constants				Young's modulus		Poisson's Ratio		Ultimate Strain		
	C_{11}	C_{22}	C_{12}	C_{66}	Y_x	Y_y	ν_x	ν_y	US_x	US_y	US_{xy}
th-CN_2	338.36	195.27	-1.54	87.14	338.35	195.26	-0.004	0.008	26	15	22
th-CP_2	170.14	54.00	15.42	21.61	168.75	49.60	0.09	0.28	17	27	18
th-CAs_2	121.80	38.70	17.30	14.63	119.34	30.96	0.14	0.45	18	27	17
th-CSb_2	86.44	27.49	13.33	7.59	84.38	21.02	0.15	0.48	17	24	16

are broken in the elevated temperatures, and the original skeleton of the structures is preserved. It should be mentioned that the computational considerations limit the AIMD simulations to a few ps, which is a short interval in real conditions, but it can provide an insight into the system's thermal stability, especially structural response to thermal shock.

3.2.2.4 Mechanical stability

According to the Born-Huang elastic stability criteria [62], the prerequisites of the mechanical stability of a system are $C_{11}C_{22}$-$C_{12}^2 > 0$ and $C_{66} > 0$, where C_{11}, C_{22}, C_{12}, and C_{66} are the elastic stiffness constants. These constants can be calculated by fitting the second derivative of the strain energy per unit area into a function of the in-plane strains using the following equation,

$$E_s(\varepsilon) = \frac{1}{2}C_{11}\varepsilon_x^2 + \frac{1}{2}C_{22}\varepsilon_y^2 + C_{22}\varepsilon_x\varepsilon_y + 2C_{66}\varepsilon_{xy}^2 \tag{3.2}$$

in case of uniaxial strain along x-direction (where $\varepsilon_y = \varepsilon_{xy} = 0$),

$$E_s(\varepsilon) = \frac{1}{2}C_{11}\varepsilon_x^2 \tag{3.3}$$

for uniaxial strain along y-direction (where ε_x=ε_{xy}=0),

$$E_s(\varepsilon) = \frac{1}{2}C_{22}\varepsilon_y^2 \tag{3.4}$$

if we apply biaxial strain (where ε_x=ε_y and $\varepsilon_{xy} = 0$),

$$E_s(\varepsilon) = (\frac{1}{2}C_{11} + \frac{1}{2}C_{22} + C_{12})\varepsilon_x^2 \tag{3.5}$$

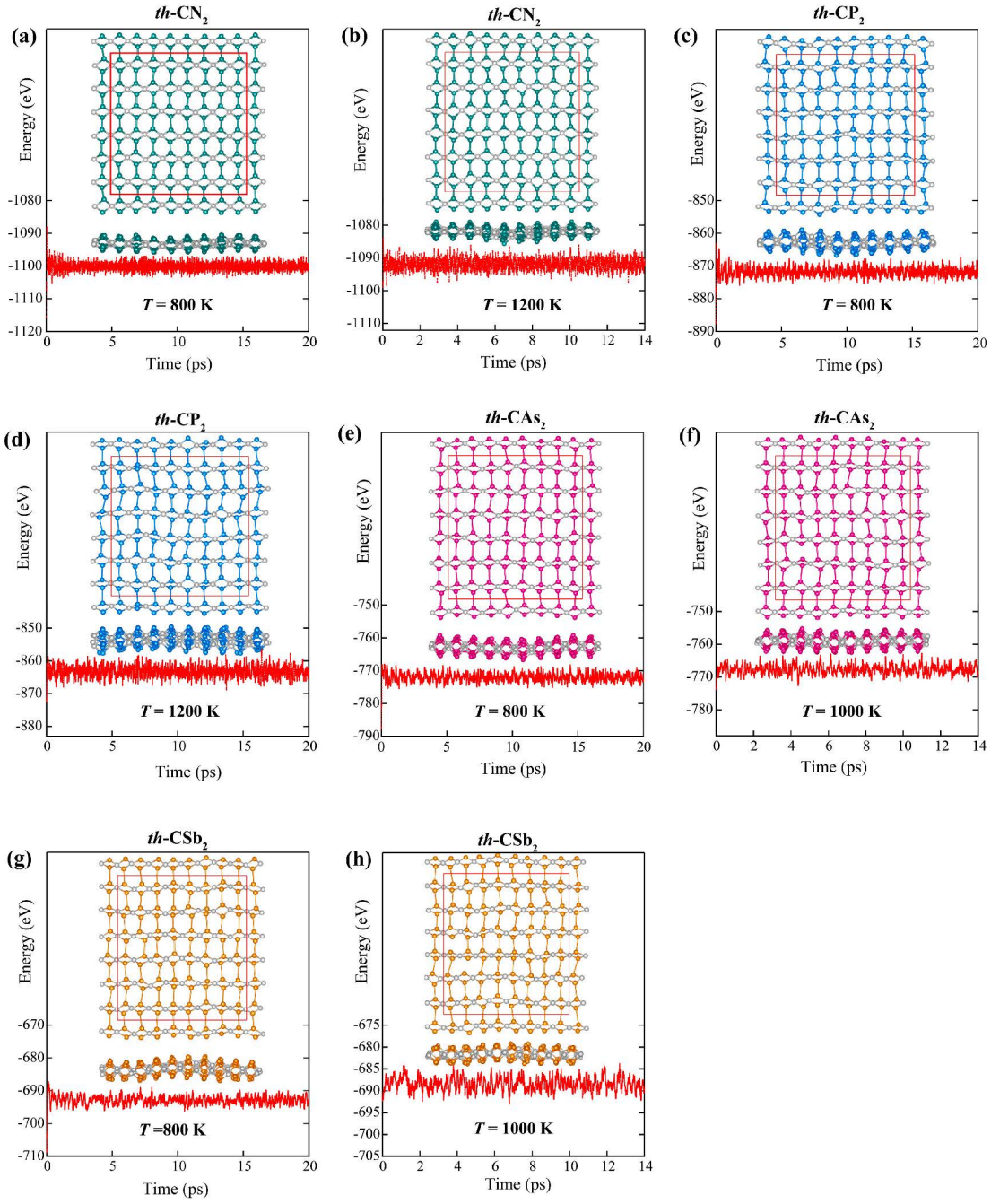

Figure 3.4: Variation of the total potential energy of *th*-CX_2 compounds (X = N, P, As and Sb) during the AIMD simulations at elevated temperature for a period of 20 ps. The insets are snapshots of the atomic structures at the end of simulations. The gray, green, blue, pink, and orange balls represent C, N, P, As, and Sb atoms, respectively.

and finally in case of shear strain (where ε_x=ε_y=0),

$$E_s(\varepsilon) = 2C_{66}\varepsilon_{xy}^2 \tag{3.6}$$

where E_s is the strain energy per unit area, ε_{xy} is the infinitesimal shear stress, and ε_x and ε_y are the infinitesimal uniaxial strains along a and b lattice vectors, respectively. Therefore, from Eq. (3), C_{11} can be obtained by applying strain along lattice vector a (where ε_x=$\frac{a-a_0}{a_0}$ and ε_y=0). Similarly, from Eq. (4), C_{22} can be calculated by applying uniaxial strain along lattice vector b (where ε_y=$\frac{b-b_0}{b_0}$ and $\varepsilon_x = 0$). Having C_{11} and C_{22}, to find C_{12} from Eq. (5) biaxial strain can be employed (where $\varepsilon_x = \varepsilon_y$). Finally, the value of C_{66} can be achieved in the shear strain condition. To extract the elastic stiffness constants, uniaxial, biaxial, and shear strains were applied in a range of -2% to 2% with an increment of 0.5%. In the case of uniaxial strains, a perpendicular stress component will appear in the system due to Poisson's effect. This stress was relieved by structural relaxation along its axis. Variation in the strain energy *vs* strain is demonstrated in Fig. 3.5, and the extracted constants are listed in Table 3.3. It can be seen that the mechanical stability criteria are satisfied for every member of the *th*-CX_2 family.

3.2.3 Mechanical properties

Having secured that all members of *th*-CX_2 family have energetic, dynamical, thermal, and mechanical stability, we investigated the most important strain-dependent mechanical properties of these materials, including in-plane Young's modulus (Y), Poisson's ratio (ν), and ultimate strain (US). As it is shown in the following sections, the intrinsic anisotropy in the geometric structure of *th*-CX_2 gives rise to direction-dependent mechanical properties.

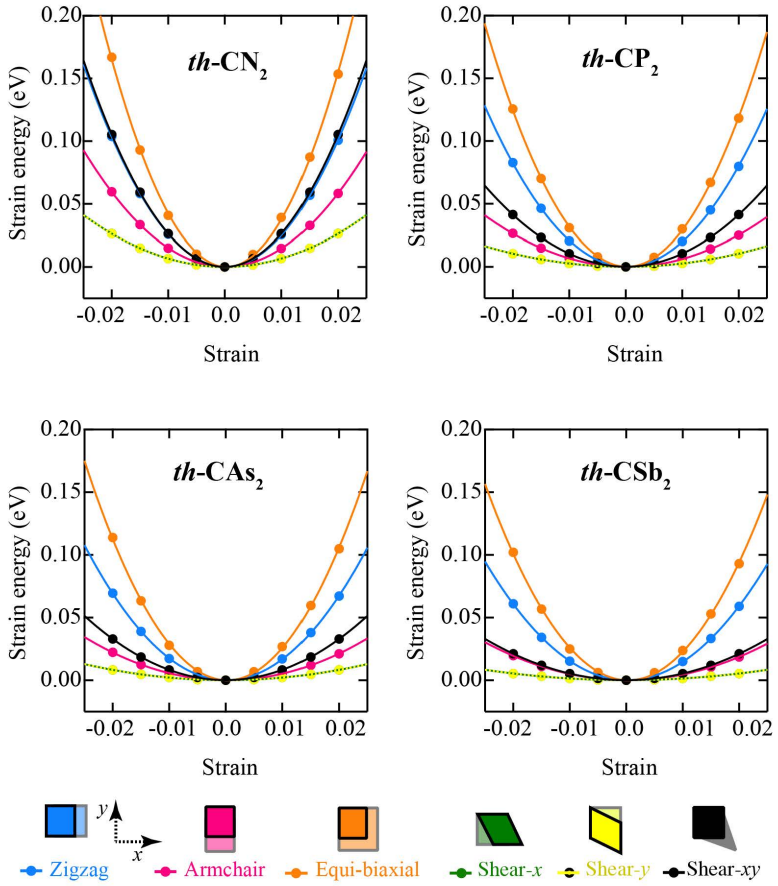

Figure 3.5: Calculated strain energy of *th*-CX_2 compounds (X = N, P, As and Sb) with respect to various applied strains: uniaxial strain along the zigzag and armchair directions, equi-biaxial strain, and shear strains.

3.2.3.1 Young's modulus

Young's modulus is the slope of the stress-strain curve in the elastic region which defines the stiffness of the material. In other words, a material with high stiffness deforms slightly under stress. Since structural deformation can dramatically change the electronic and optical properties, stiffness is of great importance in the study of 2D materials. The intrinsic anisotropy in the geometric structure of *th*-CX_2 gives rise to direction-dependent Young's modulus. Here, through the following expression, we represent the angle-dependent Young's modulus of *th*-CX_2 compounds,

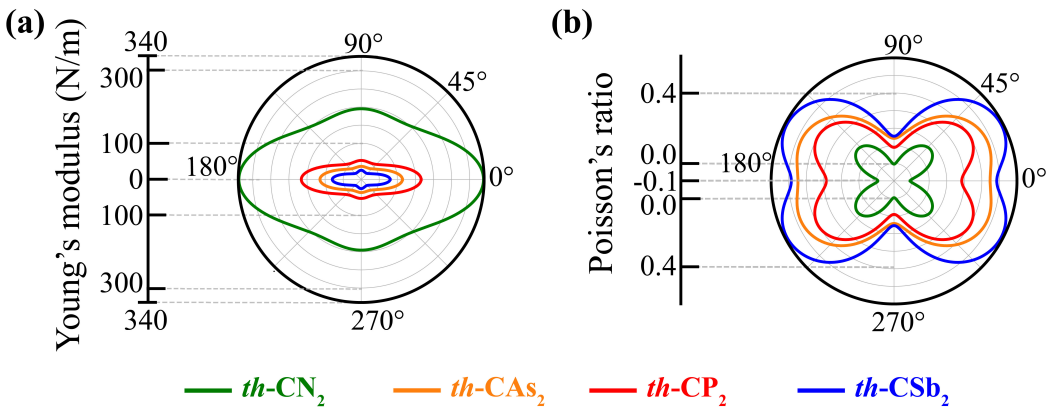

Figure 3.6: The angle-dependent evolution of (a) Young's modulus (Y_θ) and (b) Poisson's ratio (ν_θ) in *th*-CX_2 compounds.

$$Y_\theta = \frac{C_{11}C_{22} - C_{12}^2}{C_{11}A^4 + (\frac{C_{11}C_{22}-C_{12}^2}{C_{66}} - 2C_{12})A^2B^2} \tag{3.7}$$

where A and B stand for $\sin(\theta)$ and $\cos(\theta)$, respectively. In Fig. 3.6 (a), Young's modulus of *th*-CX_2 compounds *vs* in-plane angle (θ) is presented. Other than the intrinsic asymmetry of the structure, the unsimilarity between the strength of the dominant bonds in the armchair and zigzag directions directly affects the stiffness anisotropy. This difference stems from the variation in bond length and hybridization of states. In the *th*-CX_2 structures, along the zigzag direction ($\theta = 0°$ and due to reflection symmetry $\theta = 180°$), where C−X bonds are dominant, materials exhibit superior stiffness compared to the armchair direction ($\theta = 90°$ and due to reflection symmetry $\theta = 270°$), where X−X bonds are dominant. The numerical value of Young's modulus of *th*-CX_2 along $\theta = 0°$ (denoted as Y_x) and $\theta = 90°$ (denoted as Y_y) directions are listed in Table 3.3. For sake of comparison, Young's moduli of similar structures are summarized in Table 3.2. It can be seen that Young's modulus of the *th*-CN_2 (338 N/m) is comparable with that of graphene (345 N/m) [63], and outweighs that of PG (264 N/m) [9], and penta-CN_2 (264 N/m) [17]. Moreover, the maximum Young's modulus of *th*-CP_2 (169 N/m), *th*-CAs_2 (119 N/m), and *th*-CSb_2 (84 N/m) are almost three, three, and ten times of Young's moduli of their penta counterparts (60, 37, and 9 N/m [18], respectively).

3.2.3.2 Poisson's ratio

Poisson's ratio (PR) defines a material's strain behavior along a direction perpendicular to that of the applied stress, and thus it plays an important role in the strain engineering of the properties of a material. Generally, materials possess positive PR, getting thinner upon tensile and thicker under compressive stresses. On contrary, materials with negative PR (known as auxetic) are very rare, which can offer exotic mechanical properties [64, 65]. Similar to other mechanical properties of the *th*-CX_2 compounds, Poisson's ratio also exhibits a direction-dependent behavior due to the intrinsic anisotropy of the structure. Here, the angle-dependent Poisson's ratio of the *th*-CX_2 compounds was investigated through the following equation,

$$\nu(\theta) = \frac{C_{12}(A^4 + B^4) - (C_{11} + C_{22} - \frac{(C_{11}C_{22} - C_{12}^2)}{C_{66}} - 2C_{12})A^2B^2}{C_{11}A^4 + C_{22}B^4 + (\frac{(C_{11}C_{22} - C_{12}^2)}{C_{66}} - 2C_{12})A^2B^2} \tag{3.8}$$

where A and B stand for $\sin(\theta)$ and $\cos(\theta)$, respectively. The resulted graph of ν *vs* θ is presented in Fig. 3.6 (b), and the numerical value of Poisson's ratio along $\theta = 0°$ (denoted as ν_x) and $\theta = 90°$ (denoted as ν_y) directions are listed in Table 3.3. It can be seen that the minimum value of ν takes place along the armchair direction ($\theta = 90°$), and the maximum locates within the range of $0° < \theta < 45°$. The PR variation of the system is also dependent on the atomic species. As the atomic number increases, the average value of PR shows an increasing trend. Along zigzag direction, *th*-CN_2 has a negative PR, categorizing this 2D material as one of the rare auxetic materials with applications in biomedical and aerospace industries [66]. Recently, Q. Wei *et al.* [67] studied mechanical properties of *th*-CN_2, where detailed information about its auxetic behavior can be found.

3.2.3.3 Ultimate strain

Another mechanical feature of a 2D material, which is of great importance is ultimate tensile strength (UTS), and its corresponding strain, known as ultimate

strain (US). During the strain engineering of a 2D material, extreme strains can be imposed into the system. If the material lacks the proper US, its structural integrity can be damaged, and the desired performance cannot be achieved. To investigate the US of *th*-CX_2, we employed a 2×2×1 supercell and measured the stress imposed into the system upon various axial tensile strains (zigzag, armchair, and equi-biaxial). The stress-strain curve for *th*-CX_2 compounds is depicted in Fig. 3.7 (a-d), where UTS is the maximum strength that the system tolerates right before the failure. The percentage of strain at the US is indicated by the vertical dashed line, and for sake of comparison, the obtained US values for zigzag, armchair, and equi-biaxial strains (denoted by US^x, US^x, and US^{xy}, respectively) are summarized in Table 3.3. From the stress-strain curves, it can be noted that *th*-CP_2, *th*-CAs_2, and *th*-CSb_2 compounds undergo plastic deformation upon tensile strain along the armchair direction before reaching the UTS point. We further probed the atomic origin of this plastic behavior. By comparing the bond lengths in the elastic and plastic regions of curves (Fig. 3.8), we found that the main reason behind the plastic behavior of the $th-CX_2$ compounds under armchair strain is the capability of X−X bonds, which are oriented along the armchair direction, for tolerating significant elongations without detaching. In the case of strain along the zigzag direction, C−X bonds elongation mainly compensate the strain applied to the structure. These bonds elongate linearly up to the UTS point and after this point, the slope of the curve decreases, showing the bond-breaking mechanism at the UTS point. In the case of armchair strain, the X−X bonds elongation is not linear up to UTS point, and between yield strength point and UTS, their expansion accelerates, indicating a plastic behavior. Finally, after the UTS point, the rate of elongation changes which shows their detachment. In the case of equi-biaxial strain, we have a combination of the previous mechanisms, where the change in the ratio of bond elongation clearly specifies the UTS point. The US of graphene, PG, and *th*-C was reported to be 27% [68], 21% [9], and 32% [16], respectively. It can be seen that *th*-CX_2 compounds exhibit ultrahigh ultimate strain, comparable with that of graphene, and outweighing that of PG, satisfying the prerequisite for strain engineering of electronic and optical properties, which will be discussed in the following sections.

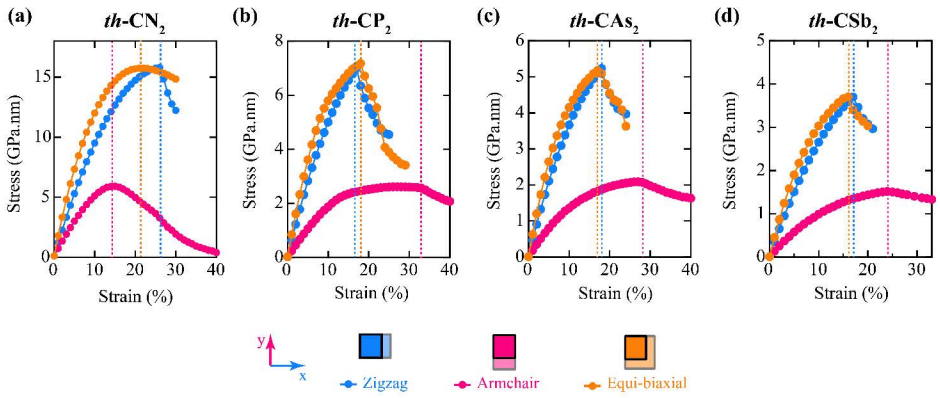

Figure 3.7: The *th*-CX_2 compounds stress-strain curves for uniaxial tensile strain along zigzag and armchair directions, and equi-biaxial tensile strain.

3.2.4 Electronic properties

Since the PBE approach underestimates the band gap energies, the electronic band structures of the *th*-CX_2 compounds were calculated through HSE06 functional along high symmetry lines of the BZ, and the results are represented alongside their corresponding orbital decomposed projected density of states (PDOS) in Fig. 3.9 (a-d), where band structure without including the spin-orbit coupling (SOC) effect is shown by dashed lines, and colored lines are related to SOC included band structure. For comparison purposes, the band gap energies for both PBE and HSE06 methods are listed in Table 3.1. It can be seen that except for *th*-CN_2 which has an insulating nature with a band gap of 4.57 eV, all the band gaps lie within the semiconducting range, promising potential for applications in solar-cell and photocatalysis. Although all the band gaps are indirect, in the case of *th*-CP_2 and *th*-CAs_2 the energy difference between direct and indirect gaps are so narrow (0.04 and 0.005 eV, respectively) that their band gap nature can be considered quasi-direct and direct, respectively. Besides, their 2.12 and 2.31 eV band gaps are comparable with that of *th*-C (2.64 eV), making them a competitive alternative of the *th*-C, as one of the best options for photocatalysis applications. It can also be seen that in SOC included calculations, although band splitting takes place due to degeneracy lift, the band gap width and band edge alignments only change marginally (in the order of meV). Based on PDOS plots, it can be inferred that in the *th*-CN_2, the valance band states mainly belong

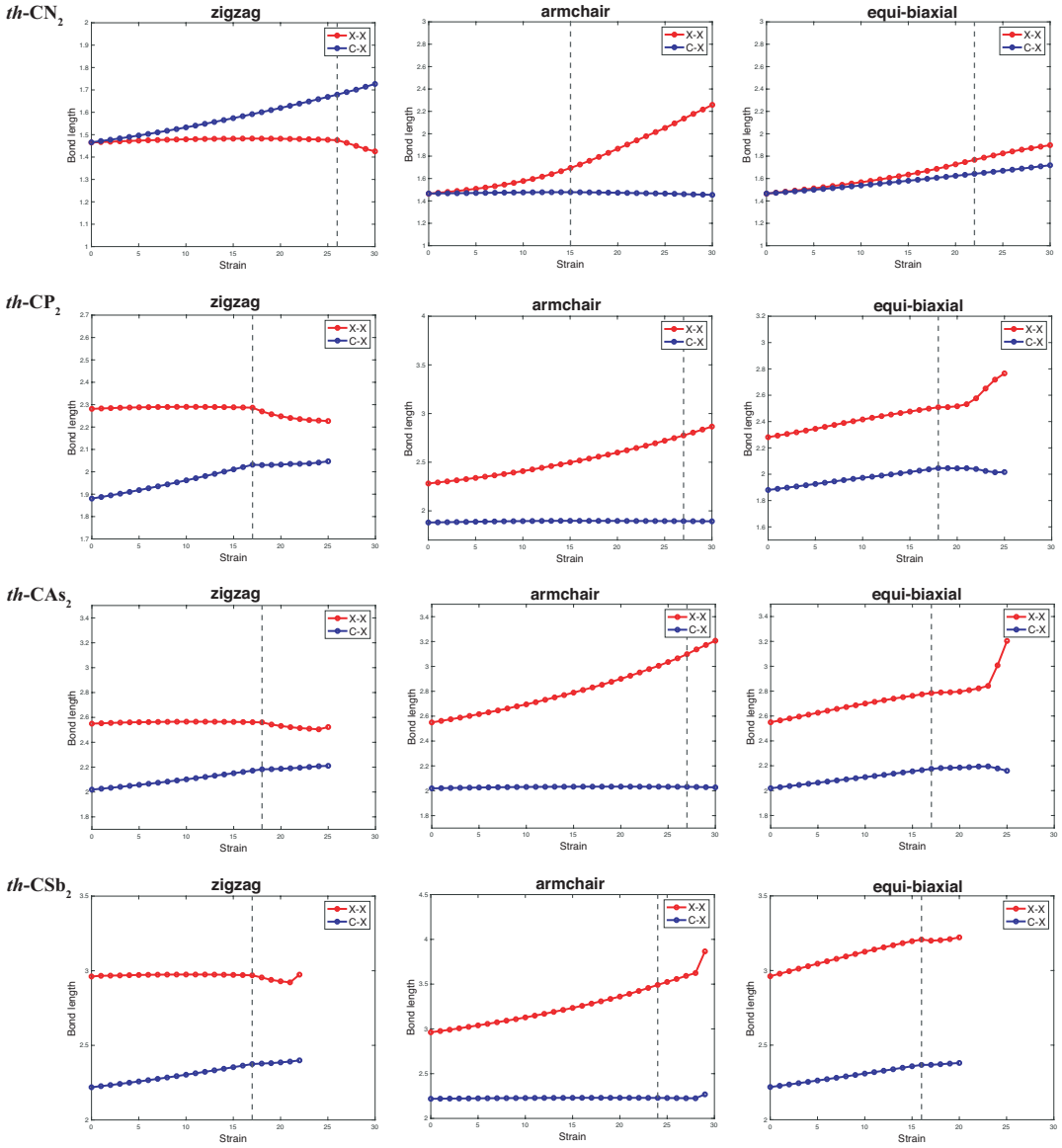

Figure 3.8: The variation of X−X and C−X bond lengths in the *th*-CX_2 structures under zigzag, armchair, and equi-biaxial strains. X−X and C−X bond lengths are shown by red and blue lines, respectively. The UTS points are specified by dashed black line.

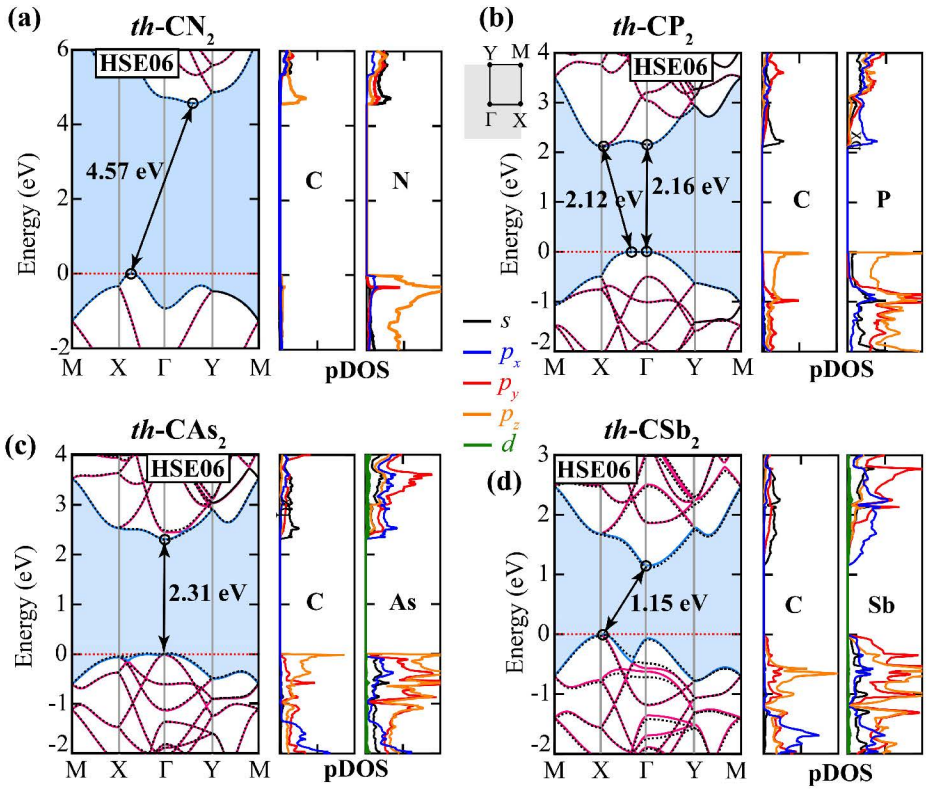

Figure 3.9: Electronic band structure of *th*-CX_2 compounds obtained from the HSE06 functional. The band gap energies between valence band maximum (VBM) and conduction band minimum (CBM) are depicted in the black arrows. The fundamental band gap between VBM and CBM is shaded in blue. The Fermi level is set to zero, and demonstrated by the dashed black line Dashed bands are calculated without including SOC effect, and colored bands are SOC included. The orbitally decomposed projected density of states (PDOS) plots are depicted next to their corresponding band structure.

to p_z orbitals of N atoms, and both p_z of C atoms and sp^3 orbitals of N contribute to the valance band. The orbitals' contribution to valence and conduction bands in *th*-CP_2 and *th*-CAs_2 show similarities, where the valence band is mostly made of both C and X atoms p_z states, and the conduction band is a combination of s orbital of C and p_x of X. In the case of *th*-CSb_2, the valence band is mostly made of p_y orbital states of Sb, and the conduction band mainly consists of s orbital of C and p_x orbital of Sb.

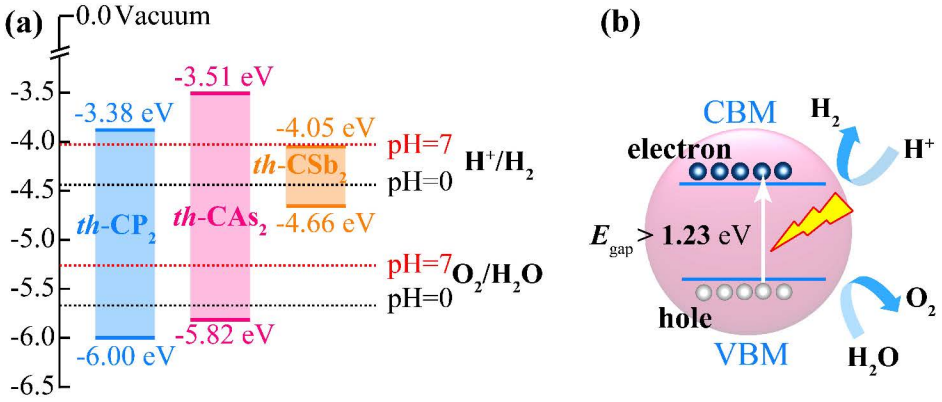

Figure 3.10: (a) Location of the band-edges in *th*-CP_2, *th*-CAs_2, and *th*-CSb_2 with respect to vacuum level obtained from HSE06 functional. The dashed lines are aligned to the oxidation/reduction potentials of water splitting, where black denotes pH = 0 and red shows pH = 7 cases. (b) The minimum band gap energy, required to provide enough photo-generated energy for the splitting of the water molecules.

3.2.4.1 Photocatalytic properties

To have an efficient photocatalyst for water splitting, a semiconductor needs to satisfy several prerequisites simultaneously. Firstly, the band gap energy should be less than 3 eV to have the optimum solar light absorption. Secondly, to be able to provide enough energy to break covalent bonds of water, the band gap energy must exceed 1.23 eV (the free energy of water splitting)(see Fig. 3.10 (b)). The third crucial requirement is the suitable location of band edges with respect to the oxidation/reduction potential of water splitting. In other words, the valence band edge location in the energy spectrum needs to be lower than the oxidation potential of O_2/H_2O (-5.67 eV + pH $\times$ 0.059 eV), and the conduction band edge position must exceed the reduction potential of H^+/H_2 (-4.44 eV + pH $\times$ 0.059 eV). Photo-induced electron/hole pair will drift for an average lifetime of τ before being annihilated by an exciton pair. To secure an efficient photocatalysis process, the fourth essential feature is a prolonged average lifetime of the charge carriers. To achieve this last requirement, the photo-generated electron/hole pairs should get separated to prevent quick recombination of them, and it is the difference in the relative drift velocities (υ_d) of electron and hole that induces this separation. Mobility, which itself is a function of effective mass, has a direct

relation with drift velocity ($\upsilon_d = \mu E$, where E is the electric field). Accordingly, semiconductors that have inequivalent electron and hole mobilities offer a longer charge carrier lifetime. Moreover, a system with direction-dependent mobility can also further facilitate charge carrier separation. Here, we propose the 2D *th*-CP_2 and *th*-CAs_2 as two suitable candidates that ideally satisfy all of the above mentioned requirements. The 2.12 (quasi-direct) and 2.31 eV (direct) energy band gaps of *th*-CP_2 and *th*-CAs_2, respectively, settle perfectly within the $1.23 < E_{gap} < 3$ eV range, which offers the optimum solar light absorption and fulfill the energy demand for splitting water molecules, simultaneously. As it is summarized in Table 3.1 and demonstrated in Fig. 3.10 (a), the VBM band edge of *th*-CP_2 and *th*-CAs_2 with energies of -6.00 and -5.81 eV, respectively, are accurately settled below the oxidation potential of water (for a whole range of pH = 0 to pH = 7). Concomitantly, the CBM band edge of both candidates is situated above the reduction potential of water (for a whole range of pH = 0 to pH = 7). In addition to these desired features, *th*-CP_2 and *th*-CAs_2 both offer direction-dependent charge carrier mobility, where hole mobilities exhibit over 1000 and 690% anisotropy, and electron mobilities show over 1800 and 2700% anisotropy between zigzag and armchair directions for *th*-CP_2 and *th*-CAs_2, respectively. Moreover, a notable divergence is also detectable between the electron and hole mobilities, where for instance, over 4100 and 720% differences exist between the electron and hole mobilities of *th*-CP_2 and *th*-CAs_2, respectively, along zigzag direction. Thus, we can firmly claim that *th*-CP_2 and *th*-CAs_2 are excellent candidates for photocatalytic water splitting applications. In the case of *th*-CSb_2, although the CBM has a proper alignment, the VBM position is above the oxidation potential of water splitting, reducing the photocatalytic efficiency of this material for water splitting (see Fig.3.10 (a)). Finally, it should be mentioned that since *th*-CN_2 does not have the proper band alignment with the redox potential of water, it is not a suitable candidate for the splitting of water.

3.2.4.2 Effective mass and carrier mobility

To achieve a better insight into the charge carrier migration properties, the effective mass (m^*) and carrier mobility (μ) of the *th*-CX_2 compounds are investigated. The effective mass was obtained through fitting a parabolic function into the electronic band structure via the following equation,

$$m^* = \hbar^2 (\frac{d^2E(k)}{dk^2})^{-1} \tag{3.9}$$

where $\hbar$ is the reduced Planck constant, k is the wave-vector, and $\frac{d^2E(k)}{dk^2}$ is the second derivative of the energy with respect to wave vector in the minimum of the conduction band (for electrons) or the maximum of the valence band (for holes). The electron and hole effective masses with respect to free-electron mass (m_0) along the Γ-X (denoted by m_x^*) and Γ-Y (denoted by m_y^*) are listed in Table 3.4. It can be seen that in all *th*-CX_2 compounds the effective masses are inequivalent and direction-dependent. This anisotropy is also manifested in the unequal curvature of band dispersion around the VBM and CBM points. This anisotropy reaches its apex in the hole effective mass of the *th*-CAs_2 and with a 755% difference between its values along the zigzag and armchair directions. The *th*-CP_2 also exhibits significant anisotropy of 673% in its hole effective mass along the zigzag and armchair directions. Moreover, in both of these two structures, the effective masses of electrons are significantly higher than that of holes. We further investigated the charge carrier mobilities along the Γ-X (symbolized by μ_x^{2D}) and Γ-Y (symbolized by μ_y^{2D}) directions, using the modified Bardeen-Shockley's formula for anisotropic 2D semiconductors [69],

$$\mu_i = \frac{e\hbar^3 C_i}{K_B T m_i^* m_d E_{1i}^2} \tag{3.10}$$

where i determines the transport direction (x and y stand for zigzag and armchair, respectively), m_i^* is the effective mass along i direction, and m_d is the geometric mean of effective masses along x- and y-direction ($\sqrt{m_x^* m_y^*}$). Temperature is considered to be $T = 300\,\mathrm{K}$. The E_{1i} is the deformation potential constant of the

carrier, obtainable from the following equation,

$$E_{1i} = \frac{\Delta E}{(\frac{\Delta l}{l_0})} \tag{3.11}$$

where ΔE is the variation in the energy of the CBM and VBM bands under small strains (0.5% in our calculations) (see Fig. A(1-4) in Appendix). The C_i in Eq. 10 is the in-plane stiffness constant, calculated based on the following formula, and reported in Table 3.4,

$$C_i = 2(\frac{E_i - E_0}{A_0})(\frac{\Delta l}{l_0})^{-2} \tag{3.12}$$

where E_i is the total energy of the unitcell after deformation, E_0 and A_0 are the total energy and area of the unitcell, respectively. Since charge carrier mobility depends on anisotropic factors, such as effective mass, one can see that the *th*-CX_2 compounds have highly direction-dependent carrier mobilities.

In Eq. 10, it was assumed that mobility is only dependent on the deformation potential and in-plane stiffness constant along the migration direction. In real 2D anisotropic materials, however, mobility is under influence of scattering events from all directions. This oversimplification can lead to an overestimation of the anisotropic behavior of 2D materials. An improved version of the mobility formula was proposed by Lang et al. [70] as follows,

$$\mu_i = \frac{e\hbar^3(\frac{5C_i+3C_j}{8})}{K_B T m_i^* m_d(\frac{9E_{1i}^2+7E_{1i}E_{1j}+4E_{1j}^2}{20})} \tag{3.13}$$

For sake of comparison, the results obtained from the Eq. 13 are also presented in Table 3.4. It can be noted that the results obtained using Lang et al.'s formula (Eq. 13) have two main differences compared to their corresponding values found from modified Bardeen-Shockley's formula (Eq. 10). Firstly, all mobility values resulted from Eq. 13 are lower than their counterparts obtained from Eq. 10. Secondly, the anisotropy of the mobilities obtained from Eq. 13 is lower than their counterparts calculated based on Eq. 10. These deviations stem from the consideration of the effect of electron-phonon scattering events in transpose direction, perpendicular to that of mobility measurement, implemented in Lang et al.'s formula (Eq. 13). Previous studies have shown that Eq. 10 overestimates both the carrier mobility and anisotropic ratio. Eq. 13, however, underestimates

Table 3.4: Charge carrier properties, where m_x^*/m_0 and m_y^*/m_0 are the carrier effective masses with respect to a static electron mass (m_0) along zigzag and armchair directions, C_{2D} is the elastic constant in the unit of N/m, and μ^{2D} is the carrier mobility in the unit of $cm^2V^{-1}s^{-1}$ at $T = 300$ K.

		Effective mass		In-plane stiffness		Mob. (Eq. 3.10)		Mob. (Eq. 3.13)	
Structure	Carrier type	m_x^*/m_0	m_y^*/m_0	C_{2D}^x	C_{2D}^y	$\mu_x^{2D}\times10^3$	$\mu_y^{2D}\times10^3$	μ_x^{2D}	μ_y^{2D}
th-CN_2	Hole	0.22	0.33	338.36	195.27	55.97	6.96	1323.45	582.38
	Electron	0.44	1.09	338.36	195.27	2.42	0.05	25.16	5.40
th-CP_2	Hole	9.22	1.37	170.15	54.00	0.01	1.13	0.37	3.87
	Electron	0.89	0.69	170.15	54.00	3.02	0.05	15.30	8.34
th-CAs_2	Hole	0.54	4.08	121.80	38.70	0.31	0.06	16.24	2.34
	Electron	0.58	0.88	121.80	38.70	6.79	0.33	117.89	42.51
th-CSb_2	Hole	0.19	0.71	86.44	27.49	0.59	0.28	32.38	9.97
	Electron	0.25	1.12	86.44	27.49	68.12	0.37	544.44	55.23

the carrier mobility while the anisotropy ratios obtained from this formula are in good agreement with experimental results [69]. Thus, we can predict that the experimental carrier mobility of the *th*-CX_2 compounds settle between the two reported values, and the anisotropy is close to the values obtained by Lang et al.'s method.

3.2.4.3 Strain-engineering of the band gap and band edge positions of *th*-CX_2 compounds

Numerous studies showed that tuning the electronic properties through strain-engineering can significantly increase the efficiency of the 2D semiconductors [16, 71]. Here, we investigate the effect of strain on the *th*-CX_2 compounds, and we indicate that the band gap type and energy, and the band edge locations can be systematically tailored under strain. The calculated results, using the HSE06 functional, are represented in Fig. 3.11 (a-d), for armchair, zigzag, and equi-biaxial strains within -4% and 10% range with the increments of 2%. A structural relaxation was performed at each step of straining, and the electronic properties were calculated for the relaxed structure. It can be seen that within this strain range, although band gap energies vary significantly, the semiconducting nature of the compounds is preserved and no gap closure is observed. In the case of *th*-CN_2, compressive strain tends to increase the band gap energy and tensile strain reduces this value, but even 10% tensile strain cannot bring the band

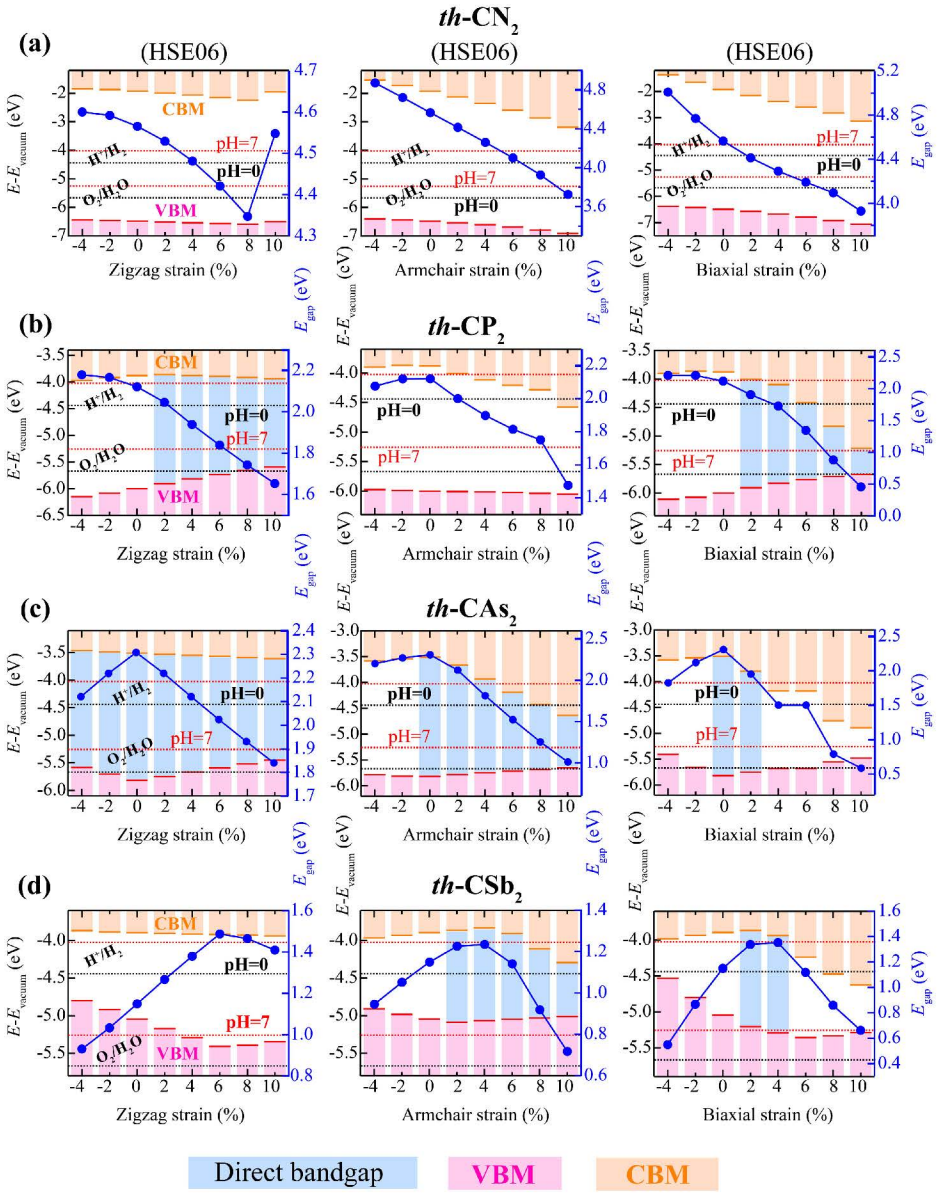

Figure 3.11: Strain engineering of the band gap and band edges alignment (with respect to the redox potential of water splitting) of *th*-CX_2 compounds, calculated via HSE06 functional, for zigzag, armchair, and equi-biaxial strains in the range of -4% to 10% (negative/positive numbers refer to as the compressive/tensile strain), with increments of 2%. The dark blue markers depict the band gap values. The valence band maximum (VBM) and conduction band minimum (CBM) positions with respect to the redox potential of water splitting are accentuated with purple and orange tints, respectively. The bright blue shadow demonstrates an indirect to direct transition of the band gaps.

gap energy to less than 3 eV, in the efficient region for the optical absorption. Besides, no indirect to direct band gap transition can be induced in this structure via strain engineering. Also, the alignment of the band edges with the redox potential of water cannot be improved under strain. Therefore, *th*-CN_2 cannot be the best candidate for the photo-induced splitting of water even in strained conditions. Previously, we demonstrated that *th*-CP_2 and *th*-CAs_2, both offer suitable features for photocatalytic water splitting in pristine conditions. These promising properties in *th*-CP_2 only miss one element to become perfect, that is the lack of a direct band gap. Although in this compound, in pristine conditions, the band gap nature can be considered quasi-direct, which guarantees their applicability in the photocatalysis process, a quasi-direct to direct transition can be induced through strain-engineering to further boost its photocatalytic efficiency. This transition occurs upon 2% zigzag and biaxial tensile strain. According to Fig. 3.11 (b), under intense biaxial tensile strain, the CBM alignment of *th*-CP_2 with reduction potential of water deteriorates. A similar trend can also be observed in the CBM alignment of *th*-CAs_2, if the armchair tensile strain exceeds 6% (see Fig. 3.11 (c)). Fortunately, band gap tunings via tensile strain along zigzag direction do not ruin the alignment of band edges with water decomposition potentials in both of these compounds. Therefore, alongside *th*-CAs_2 in pristine conditions, we can consider the strain-engineered versions of *th*-CP_2 as the optimum candidates for photocatalytic water splitting. Finally, in *th*-CSb_2, where an efficient band alignment is not achievable in pristine conditions, small tensile strains can enhance the position of the band edges with respect to redox potentials of water, and increase the band gap energy to near 1.23 eV threshold to provide enough energy for water decomposition. Besides, under tensile strains, an indirect to direct band gap transition can also be induced. Thus, a significant improvement can be achieved in photocatalytic efficiency of *th*-CSb_2 for water splitting purposes.

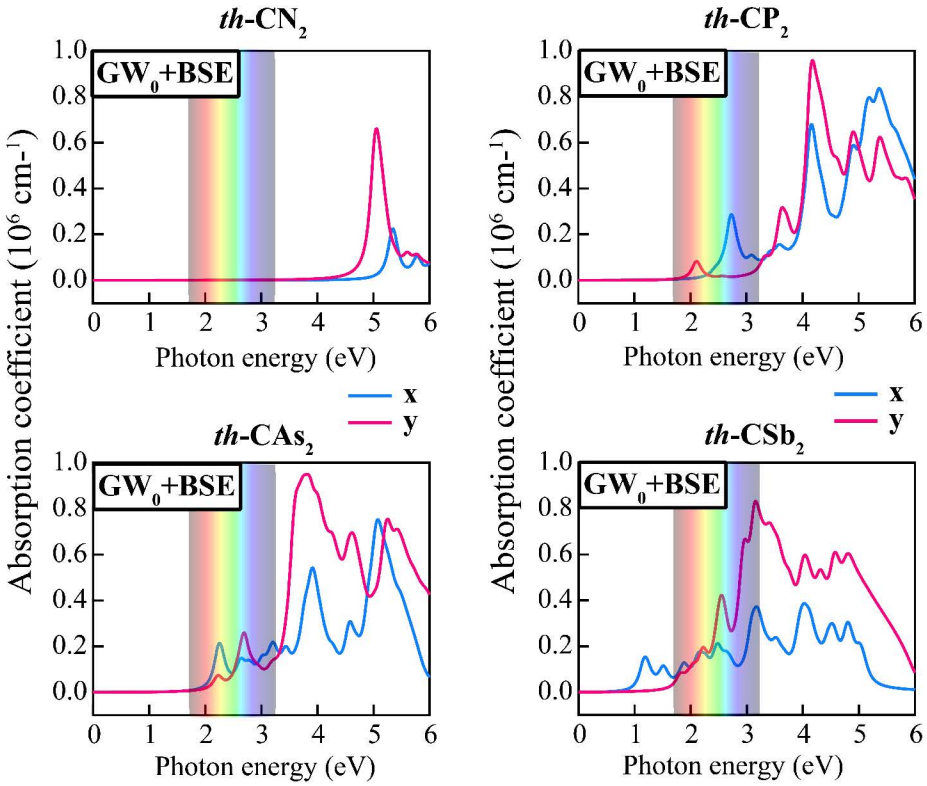

Figure 3.12: Optical absorption coefficient of *th*-CX_2 compounds along zigzag (x) and armchair (y) directions, as a function of photon energy, calculated based on the GW_0+BSE method.

3.2.5 Optical properties

To enhance photocatalytic performance, optical absorption is another factor that plays a crucial role in the photocatalytic capacity of a material. From an energetic point of view, ultraviolet light can facilitate photocatalytic activities better than visible light, since its high photonic energy is enough to overcome large energy barriers in a catalysis process. On the other hand, the ultraviolet part of the solar spectrum is only limited to 4%. Thus, a photocatalyst material needs to be also able to absorb a significant fraction of the visible light (which covers around 43% of the solar incident beams, reaching the earth's surface). As it was mentioned, a suitable semiconductor for application in photocatalytic water splitting should have a band gap of more than 1.23 eV, which shifts the absorption peaks towards the ultraviolet region of the light spectrum. Thus, candidates with partial light

absorption in the visible range, such as TiO_2, are the best viable options for this purpose [72]. The light-harvesting performance of the *th*-CX_2 compounds was evaluated through the state-of-the-art GW_0+BSE method, and the resulted optical absorption spectrum *vs* the light energy are presented in Fig. 3.12. Here, the polarization vectors are considered parallel to the layer plane (x is along the zigzag edge and y is along the armchair edge). It can be seen that all of the 2D *th*-CX_2 compounds exhibit an anisotropic optical absorption, which can be exploited in optoelectronic devices to manipulate the polarization of the incident light. This anisotropic optical behavior stems from the intrinsic anisotropy of the structure, where the distribution of the charge density is direction-dependent (See Fig. 3.2). In *th*-CN_2, the absorption peaks lie out of the visible region, within the ultraviolet zone, with a strong absorption along the armchair and a weak absorption coefficient along the zigzag direction. As the atomic number of the X component increases, the absorption peaks shift towards the visible region. In *th*-CP_2 and *th*-CAs_2, the absorption graph spreads all over the ultraviolet and visible region of the light spectrum. These ideal spreads of the light absorptions, combined with the proper band gap and band alignment of these two monolayers, make them promising candidates as photocatalysts in the water-splitting process. Finally, although *th*-CSb_2 in pristine conditions is not the optimum candidate for photocatalytic water splitting due to improper band alignment, it exhibits an anisotropic absorption covering the whole spectrum from infrared to ultraviolet, where the absorption peaks are located in the visible region. Thus, the intrinsic semiconducting nature of *th*-CSb_2, combined with its wide-range optical absorption, makes this material a suitable option to be utilized in many areas of optoelectronic applications, including the photocatalytic decomposition of toxic gases.

3.3 Tetrahex Nitrides

Motivated by the exotic properties found in the *th*-CN_2, especially its auxetic behavior, we furthur investigate the properties of *th*-SiN_2. For ease of comparison, the properties of *th*-CN_2 is presented alongside *th*-SiN_2.

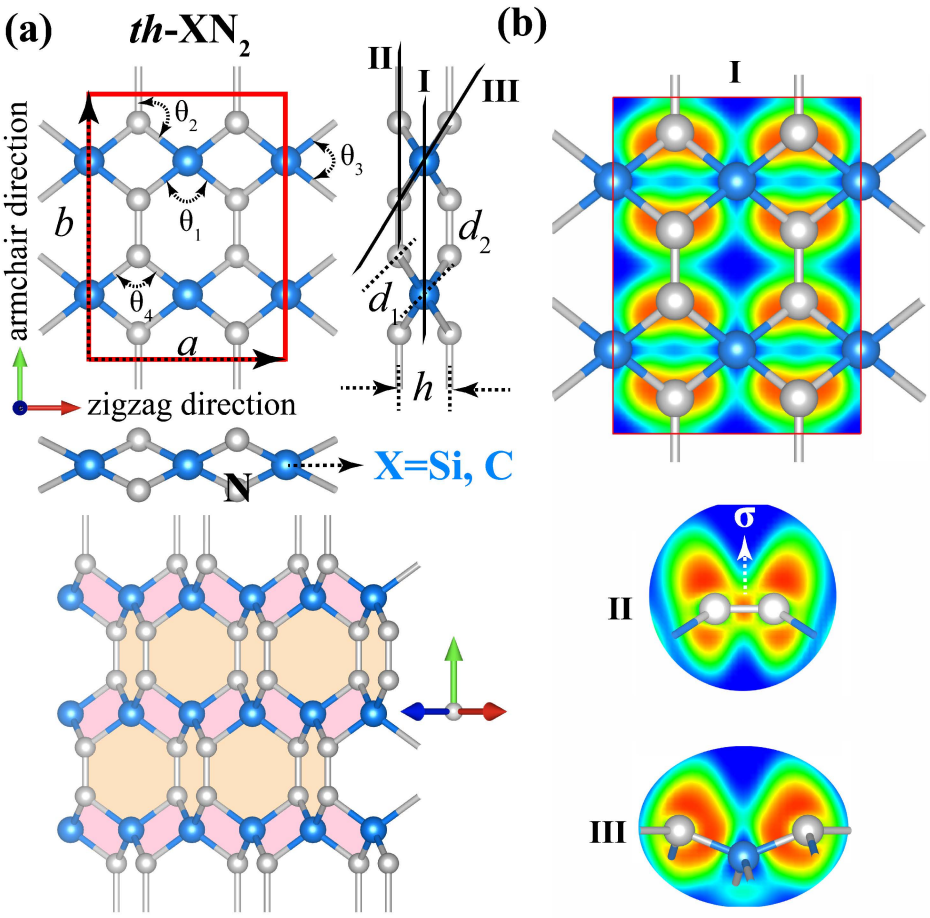

Figure 3.13: (a) Ball and stick model of the *th*-XN_2 compounds (X = Si and C) from the top, side, and tilted views, where the unitcell is depicted in the red line. Blue and gray balls represent X and N atoms, respectively. (b) The electron localization function (ELF) plots of *th*-SiN_2 from top and side views, showing the sigma nature of X−N and N−N bonds.

3.3.1 Structural properties

The structural configuration of the *th*-XN_2 compounds (where X = Si and C) is presented in Fig. 3.13 (a). Similar to the tetrahex carbides, the unitcell has an orthorhombic form, with two perpendicular and unequal lattice constants of a and b. The sequence of tetragonal and hexagonal building blocks forms a Cmme symmetry (space group number 67), where X atoms occupy the 4-fold coordinated positions, and N atoms fill the 3-fold coordinated locations. As seen, from the side view, the structure is made of three layers; one layer of X atoms is sandwiched

Table 3.5: The structural, energetic and electronic properties of the *th*-XN_2 compounds, where a and b are lattice parameters, h is the thickness, $d_{(1-2)}$ are bond lengths in unit of Å, $\theta_{(1-4)}$ are interbond angles, E_{coh} is the cohesive energy in unit of eV/atom, E_g^{PBE} and E_g^{HSE} are the band gap energies in unit of eV obtained from PBE and HSE06 functionals, respectively.

Structure	a	b	h	d_1	d_2	θ_1	θ_2	θ_3	θ_4	E_{coh}	E_g^{PBE}	E_g^{HSE}
th-SiN_2	5.10	6.91	1.30	1.75	1.45	110	125	86	93	5.05	3.26	4.53
th-CN_2	4.17	5.78	1.48	1.46	1.46	122	119	89	91	5.19	3.05	4.57

between two layers made of N atoms, and the distance between these top and bottom layers defines the thickness (h). The X−N and N−N bond lengths are denoted by d_1 and d_2, respectively. The numerical values of these structural properties are listed in Table 3.5. It can be seen that both structures have an overall similarity in their structures, with minor differences which stem from the larger atomic radius of Si compared to C. The lattice constants (a and b) in *th*-SiN_2 show an elongation in comparison to *th*-CN_2, and the Si−N bond length shows an increase compared to C−N bond. The N−N bond length, however, is almost equivalent in both compounds, which shows that the type of X atoms does not affect the nature of N−N bonds. It can be inferred that N−N has a single bond nature, since its length has compatibility with the average length of the single-bonded N−N dimers (d=1.45). The electron localization function (ELF) plots of *th*-SiN_2 are shown in Fig. 3.13 (b). Each plot (labeled by Roman numeral symbols I, II and III) is related to a crystalographic plane, specified by the same symbol in Fig. 3.13 (a). It can be seen that between bonded pairs, the electronic charge is localized in the middle zone. This form of charge localization shows the sigma nature of bonds between atoms, which is also compatible with the sp_3 orbital hybridization of X elements. A comparison between the structural properties of *th*-XN_2 compounds, and their penta−XN_2 counterparts reveals compatibility among their bond lengths [73, 17], where Si−N bond length is 1.75 and 1.74 Å in *th*-SiN_2 and penta−SiN_2, respectively, and C−N bond length is 1.46 and 1.47 Å in *th*-SiN_2 and penta−SiN_2, respectively. This resemblance implies similar bonding natures and suggests that *th*-XN_2 compounds can form from their penta−XN_2 counterparts through Stone-Wales transformation.

3.3.2 Stability

To investigate the stability of the *th*-XN_2 compounds, in the first step, we evaluated their dynamical stability based on their phonon dispersions. The phonon spectrum of *th*-SiN_2 and *th*-CN_2 are presented in the left panels of Fig. 3.14. According to harmonic approximation, imaginary vibrational frequencies indicate a disassembling tendency. Thus, to secure vibrational stability, all phonon modes must have real frequencies. One can see that no imaginary frequencies can be found in the phonon spectrum of the *th*-XN_2 structures, guaranteeing the dynamical stability of these compounds. Next to the phonon spectrum, we plotted the atom projected phonon density of states (PhDOS). The fact that highest frequency in *th*-CN_2 exceeds that of *th*-SiN_2 is a signature of robustness of C−N bonds compared to Si−N. Moreover, the maximum vibrational frequencies in *th*-SiN_2 (37 THz) and *th*-CN_2 (40 THz) is higher than penta−SiN_2 (33 THz) and penta−CN_2 (37.5 THz) [17], showing a better strength in X−N bonds of the *th*-XN_2 compounds.

In the second step, we studied the thermal stability of the *th*-XN_2 structures via $ab-initio$ molecular dynamics simulations (AIMD), performed at T=800 K for a duration of 6 ps. A relatively large supercell (4×3×1 times of the primitive cell) was employed to alleviate the periodic boundary condition constraints. The variation of potential energy *vs* time, alongside the snapshots of the ultimate structural configuration, is provided in the middle panel of Fig. 3.14. It can be seen that in both compounds potential energies only fluctuate during the simulation, and no significant deviation occurs, which implies that no structural transformation is energetically favorable even at elevated temperatures. Besides, no broken bonds or deformation can be seen in the final atomic arrangements, and the skeleton of the structures remains intact.

In the third step, the cohesive energy of the *th*-XN_2 compounds was investigated, using Eq. 3.1. The obtained cohesive energies are reported in Table 3.5. The favorable cohesive energy of *th*-CN_2 compared to *th*-SiN_2 stems from the higher bonding strength of C−N with respect to Si−N bonds [74]. A comparison

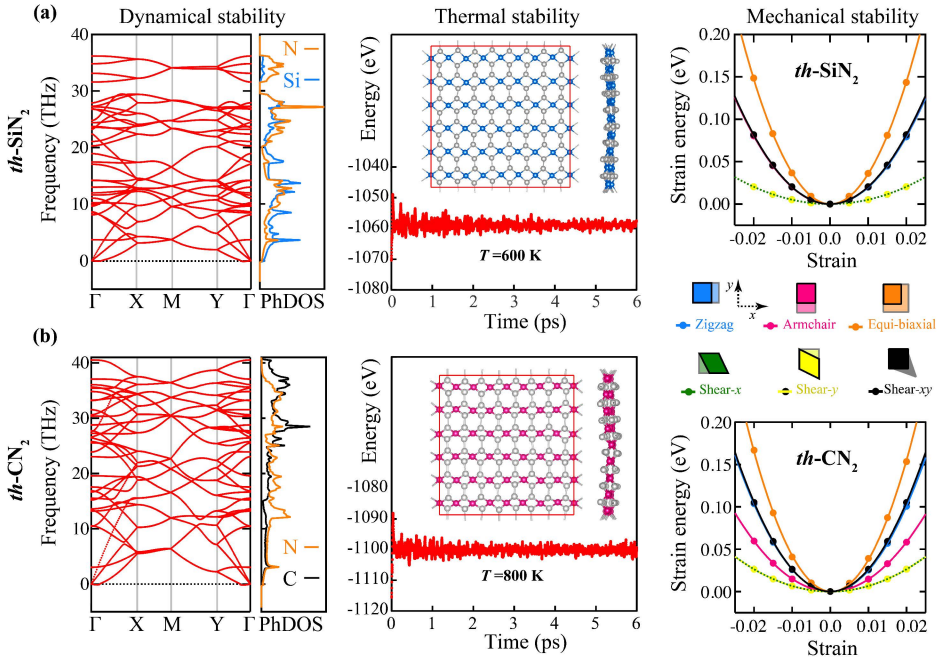

Figure 3.14: The left panels are the phonon spectrum and their corresponding PhDOS, verifying the dynamical (vibrational) stability of the *th*-XN_2 compounds. The middle panels are the evolution of the total potential energies during the AIMD simulation at T=800 K, and the insets are the snapshots of the structural configurations at the end of simulations. The right panels are the calculated strain energies with respect to various applied strains.

between the cohesive energies of these compounds with that of phosphorene (3.48 eV/atom) [61], germanene (4.15 eV/atom) [60], and silicene (4.70 eV/atom) [59] illustrates the superior bonding strength in the *th*-XN_2 structures. Although the cohesive energy value cannot verify the stability of a crystal, the fact that the *th*-XN_2 compounds have favorable cohesive energies compared to several already synthesized 2D materials is a promising sign of their stability and synthesizability.

Finally, we ensured that the *th*-XN_2 compounds have proper mechanical stability. A crystal has mechanical stability if its elastic stiffness constants fulfil Born-Huang elastic stability criteria, i.e. $C_{11}C_{22} - C_{12}^2 > 0$ and $C_{66} > 0$, where C_{ij} are elastic stiffness constants. The evolution of the strain energy under strain is demonstrated in the right panel of Fig. 3.14, and the extracted elastic stiffness constants are listed in Table 3.6. It can be seen that the Born-Huang stability criteria are satisfied by both the *th*-SiN_2 and *th*-CN_2 compounds.

Table 3.6: The mechanical properties of *th*-XN_2 structures, where C_{ij} are the elastic constants in the unit of N/m, Y_x and Y_y are Young's modulus along the zigzag and armchair directions in the unit of N/m, ν_x and ν_y are the Poisson's ratios along zigzag and armchair edges, respectively.

	Mechanical Constants				Young's modulus		Poisson's Ratio		Ultimate Strain		
	C_{11}	C_{22}	C_{12}	C_{66}	Y_x	Y_y	ν_x	ν_y	US_x	US_y	US_{xy}
th-SiN_2	182.20	184.28	-17.48	46.40	180.52	182.62	-0.096	-0.095	18	16	20
th-CN_2	338.36	195.27	-1.54	87.14	338.35	195.26	-0.004	-0.008	26	15	22

3.3.3 Mechanical properties

After assuring that both *th*-SiN_2 and *th*-CN_2 are dynamically, thermally, energetically, and mechanically stable, we studied their in-plane Young's modulus (Y), Poisson's ratio (ν), and ultimate Strain (US), as the most important strain-dependent mechanical properties. As it is shown in the following sections, the intrinsic structural anisotropy of the *th*-XN_2 compounds gives rise to direction-dependent mechanical properties.

3.3.3.1 Young's modulus

The angle-dependent Young's modulus was investigated through Eq. 3.7. The calculated Young's modulus *vs* in-plane angle is depicted in Fig. 3.15 (a), and Young's modulus numerical values along zigzag (Y_x) and armchair (Y_y) directions are listed in Table 3.6. It can be noted that the Young's modulus of *th*-CN_2 is greater than that of *th*-SiN_2 in all directions. This higher stiffness of *th*-CN_2 is caused by the presence of the C−N bonds, which have higher formation energy and thus a better strength compared to Si−N bonds. Moreover, in both compounds, Young's modulus is highly direction-dependent. *th*-SiN_2 has equivalently high stiffness along both zigzag and armchair edges, and a low stiffness along diagonal directions. In the case of *th*-CN_2, Young's modulus maximum lies along the zigzag direction, and minimum appears in diagonal orientations. The maximum of Young's modulus in both the *th*-SiN_2 (182.62 N/m) and *th*-CN_2 (338.35 N/m) compounds exceeds that of their penta counterparts (152 and 315 N/m for penta−SiN_2 and penta−CN_2, respectively [17]), and in the case of *th*-CN_2 this

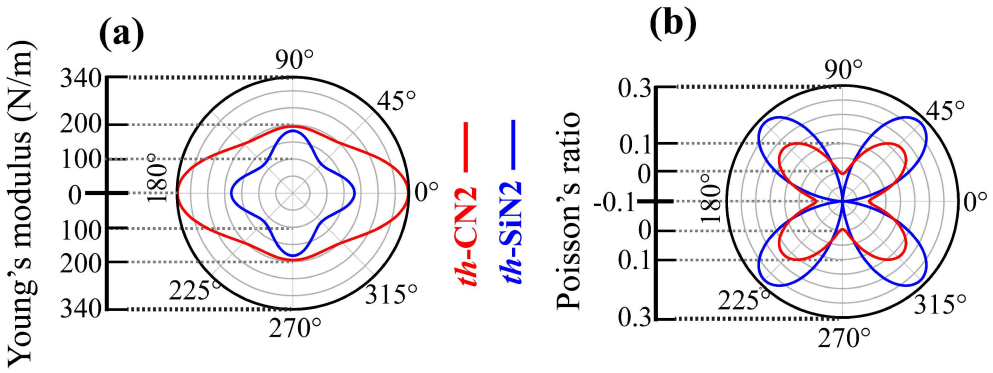

Figure 3.15: The angle-dependent evolution of (a) Young's modulus (Y_θ) and (b) Poisson's ratio (ν_θ) in the $th-XN_2$ compounds.

value is comparable to that of graphene (345 N/m [63]).

3.3.3.2 Poisson's ratio

Poisson's ratio (PR) explains a material's strain response along a direction perpendicular to that of the applied stress. In general, a crystal possesses positive PR. In this section we studied the PR response of th-SiN_2 and th-CN_2. Our calculations reveal that these compounds are among the members of the small family of materials that exhibit auxetic behavior around their equilibrium structure. Poisson's ratio (PR) along zigzag and armchair directions can be defined as $\nu_x = C_{12}/C_{11}$ and $\nu_y = C_{12}/C_{22}$, respectively. According to Table 3.6, the elastic constat C_{12} has a negative value for both th-SiN_2 and th-CN_2, which indicates the auxetic behavior of both compounds. To examine the effect of orientation on the PR response of the th-XN_2 structures, the angle-dependent Poisson's ratio was calculated via Eq. 3.8. The behavior of ν *vs* θ is visualized in Fig. 3.15 (b), and the numerical value of Poisson's ratio along θ=0° (symbolized by ν_x) and θ=90° (symbolized by ν_y) directions are reported in Table 3.6. The plot, presented in Fig. 3.15 (b), reveals not only the auxetic nature of the th-XN_2 compounds but also the anisotropy of the Poisson's ratio response. It can be seen that both compounds have positive PR values in diagonal directions, where the maximum precisely lies along the θ=45° and θ=135°. In contrast, along zigzag (θ=0°) and armchair (θ=90°) directions both compounds exhibit auxetic behavior. The scope

of auxetic response, in *th*-SiN_2, with ν_x=-0.096 and ν_y=-0.095 , is significantly higher compared to that of *th*-CN_2, with ν_x=-0.004 and ν_y=-0.008 (Recently, Wei et al. reported ν=-0.02 for *th*-CN_2 [67]). These highly negavite PR values of *th*-SiN_2 surpasses that of most of well known 2D auxetic materials such as PG (ν=-0.07 [9]), black phosphorus (ν=-0.03 [75]), borophene (ν=-0.04 [76]), and penta-B_2N_4 (ν=-0.04 [77]), making this compound highly desirable for auxetic applications. To further confirm the auxetic nature of the *th*-XN_2 structures, the evolution of bond lengths (d_1 and d_2) and thickness (h) upon uniaxial strain along zigzag and armchair edges are shown in Fig. 3.16. In an ordinary material with a positive PR value, lattice elongation along direction i will be accompanied by an expansion of the bonds oriented parallel to i and shrinkage of the bonds, oriented perpendicular to i. In the *th*-XN_2 compounds, however, independent of the direction of the lattice expansion, both the X−N and N−N bonds show an increasing trend in their lengths, which exhibits the auxetic nature of these materials. On the other hand, lattice elongation in both directions decreases the thickness of the crystals, which clears that their out-of-plane Poisson's ratio is positive. Due to the notably strong auxetic behavior of *th*-SiN_2, we further studied the effect of strain engineering on the evolution of Poisson's ratio value in this compound. Uniaxial strains along zigzag and armchair edges were applied to *th*-SiN_2 within the range of -4$\leq\varepsilon\leq$10%, with increments of 1%, and the results are presented in Fig. 3.17. In the left panels of Fig. 3.17, the total energy of structure *vs* the perpendicular lattice constant (with respect to the direction of strain) can be found. It can be seen that upon structural elongation in both zigzag and armchair directions, the optimized transversed lattice constant (b perpendicular to zigzag and a perpendicular to armchair) shows an increase under tensile strain and decrease under compressive strain. This counter-intuitive behavior clearly proves the auxetic nature of *th*-SiN_2 under any strain within the above-mentioned range. In the right panels of Fig. 3.17, the transverse strain (magnified by 1000 times) is depicted with respect to the applied strain. By definition, the slope of these curves is equal to the minus of the PR value ($\nu = -\varepsilon_i/\varepsilon_j$), where j is the direction of applied strain and i is the direction transverse to that of applied strain. Therefore, based on the plots presented in the right panels of Fig. 3.17, it can be inferred that the slopes of the curves are in agreement with the predicted auxetic

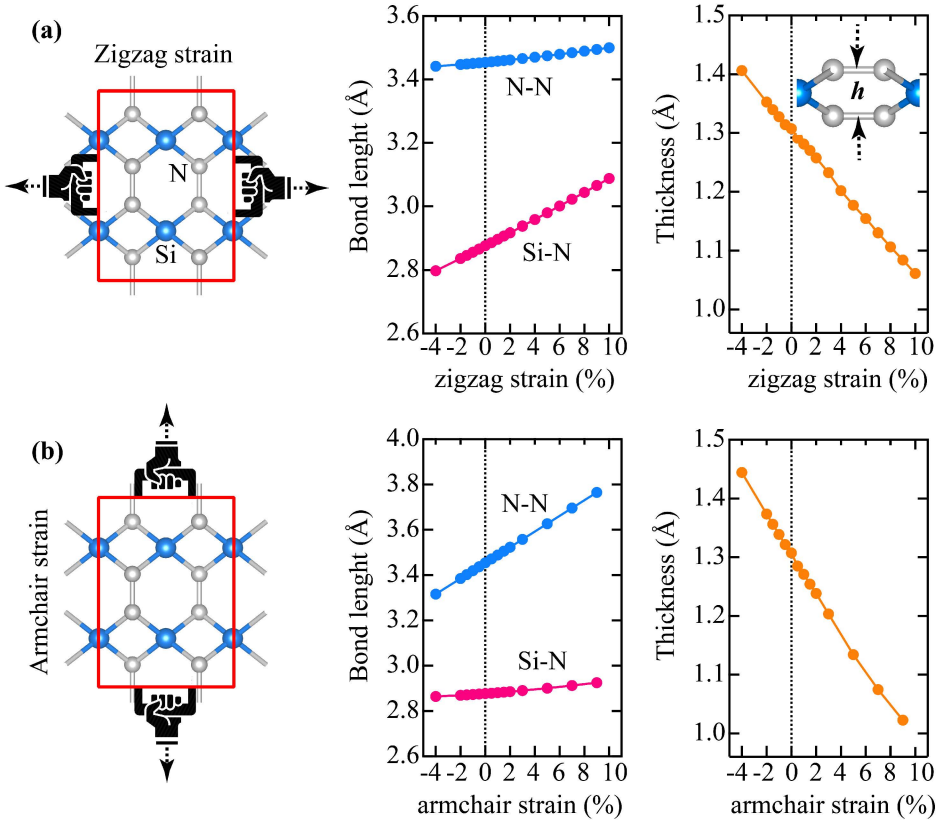

Figure 3.16: The left panels show the direction of the applied strain. The middle panels exhibit the evolution of the bond lengths under strain, where X−N and N−N correspond to d_1 and d_2, respectively. The right panels demonstrate the variation of the thickness (h) under strain.

nature of the *th*-SiN_2 compound.

3.3.3.3 Ultimate Strain

We investigated the US by employing a 2×2×1 supercell and calculating the stress imposed into the system upon various tensile strains. The obtained stress-strain curves are presented in Fig. 3.18, where the UTS point is the maximum stress that the crystal experiences right before the failure, and the percentage of strain tolerated by the system at the UTS point is US. The US under zigzag (US_x), armchair (US_y), and biaxial (US_{xy}) strains are listed in Table 3.7. It can be noted that the *th*-XN_2 compounds offer high US in all straining conditions,

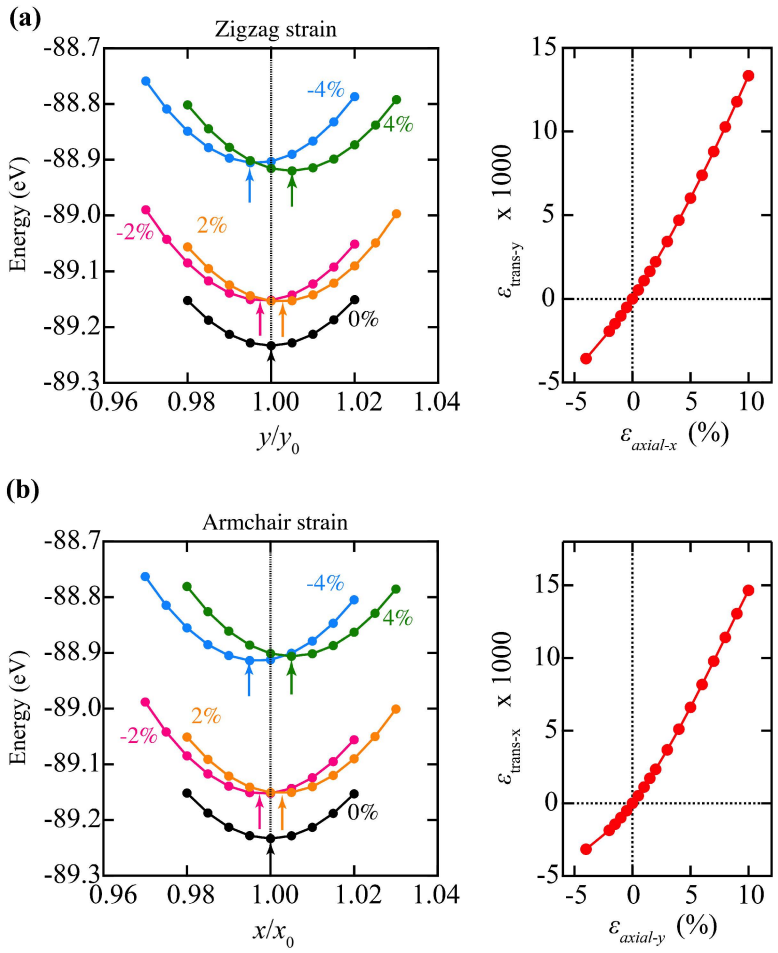

Figure 3.17: The left panels show the evolution of the lattice constant, transverse to the direction of applied strain for various strain intensities. The right panels are plots of ε_i versus ε_j, where j is the direction of applied strain and i is the direction transverse to that of applied strain.

where the maximum US appears under biaxial and zigzag strains for *th*-SiN_2 and *th*-CN_2, with 20 and 26%, respectively. These values are comparable to that of graphene (27% [68]), penta-graphene (21% [9]), and *th*−C (32% [16]). The superior US achieved in the *th*-CN_2 structure can be attributed to the higher strength of C−N compared to Si−N bonds. Moreover, the fact that none of the bonds are oriented directly along the zigzag direction, combined with the flexibility of θ_1 and θ_4 angles under strain contributes to the higher US upon strain in zigzag direction compared to armchair direction.

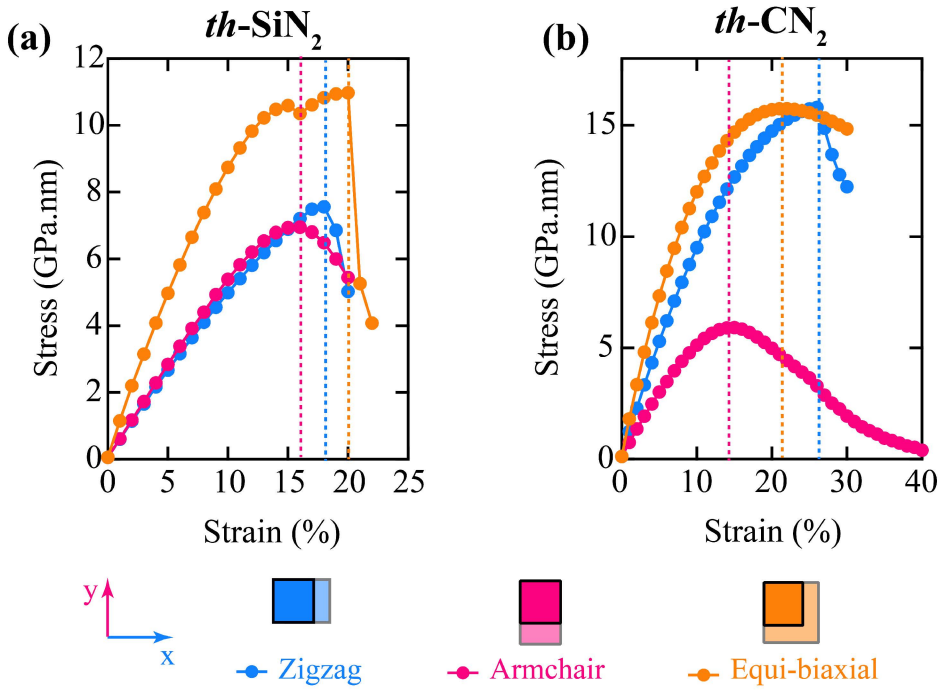

Figure 3.18: The stress-strain curves for uniaxial tensile strain along zigzag and armchair directions, and equi-biaxial tensile strain in the $th-XN_2$ compounds, where the ultimate strain (US) points are denoted by dashed lines.

3.3.4 Electronic band structures

To avoid the underestimation of the band gap energies, resulting from the PBE method, we employed HSE06 functional to study the electronic properties of the th-XN_2 compounds along high symmetry lines of the BZ. The calculated band structures alongside their corresponding projected density of states (pDOS) are presented in Fig. 3.19 (a) and (b) for th-SiN_2 and th-CN_2, respectively, and the band gap energies are reported in Table 3.5 It can be seen that both structures have wide indirect band gaps, categorizing them as insulators. In both compounds the band gap is decreased compared to their penta$-XN_2$ counterparts (5.19 and 6.53 eV for penta$-SiN_2$ and penta$-CN_2$, respectively [17]). pDOS plots reveal that in both compounds the majority of the valence band states are made of p_z orbitals of N atoms. In the case of the conduction band, however, s orbitals play important roles. While in th-SiN_2, the conduction band mostly consists of s orbitals of both Si and N atoms, in th-CN_2, the valence states are constituted

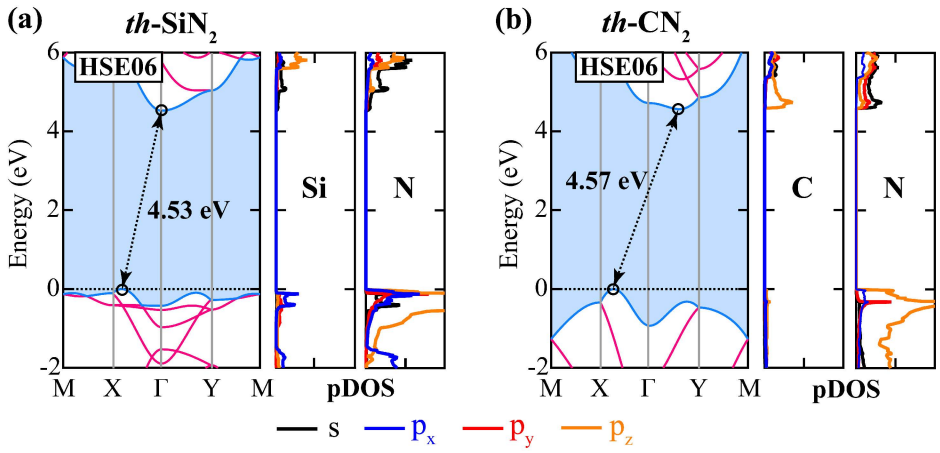

Figure 3.19: Electronic band structure of $th-XN_2$ compounds obtained from the HSE06 functional. Double-headed arrows show the position of indirect band gaps between valence band maximum (VBM) and conduction band minimum (CBM). The Fermi level is set to zero, and demonstrated by the dashed black line. The projected density of states (pDOS) plots are presented next to their corresponding band structure.

by p_z orbitals of C alongside the s orbitals of N.

3.3.5 Strain-engineering of electronic properties

Due to the high ductility of the th-XN_2 compounds, strain-engineering can be employed to tune their electronic properties. In Fig. 3.20, the evolution of electronic properties under various types of strain is demonstrated. It can be seen that in general, compressive strains tend to widen the band gap (except for compressive strain along the armchair direction in th-SiN_2), and tensile strains tend to narrow the band gap energies, generating a semiconducting nature in these compounds. The position of the valence band maximum (VBM) (blue bars) and conduction band minimum (CBM) (pink bars) with respect to the reduction/oxidation potentials of water (black and red lines for pH=0 and pH=7, respectively) are also presented in Fig. 3.20. One can see that in pristine conditions both compounds have a proper band edge alignment with redox potentials of water, and under strain, these alignments are preserved, manifesting a potential for application in the photocatalytic splitting of water. However, to have an efficient photocatalyst,

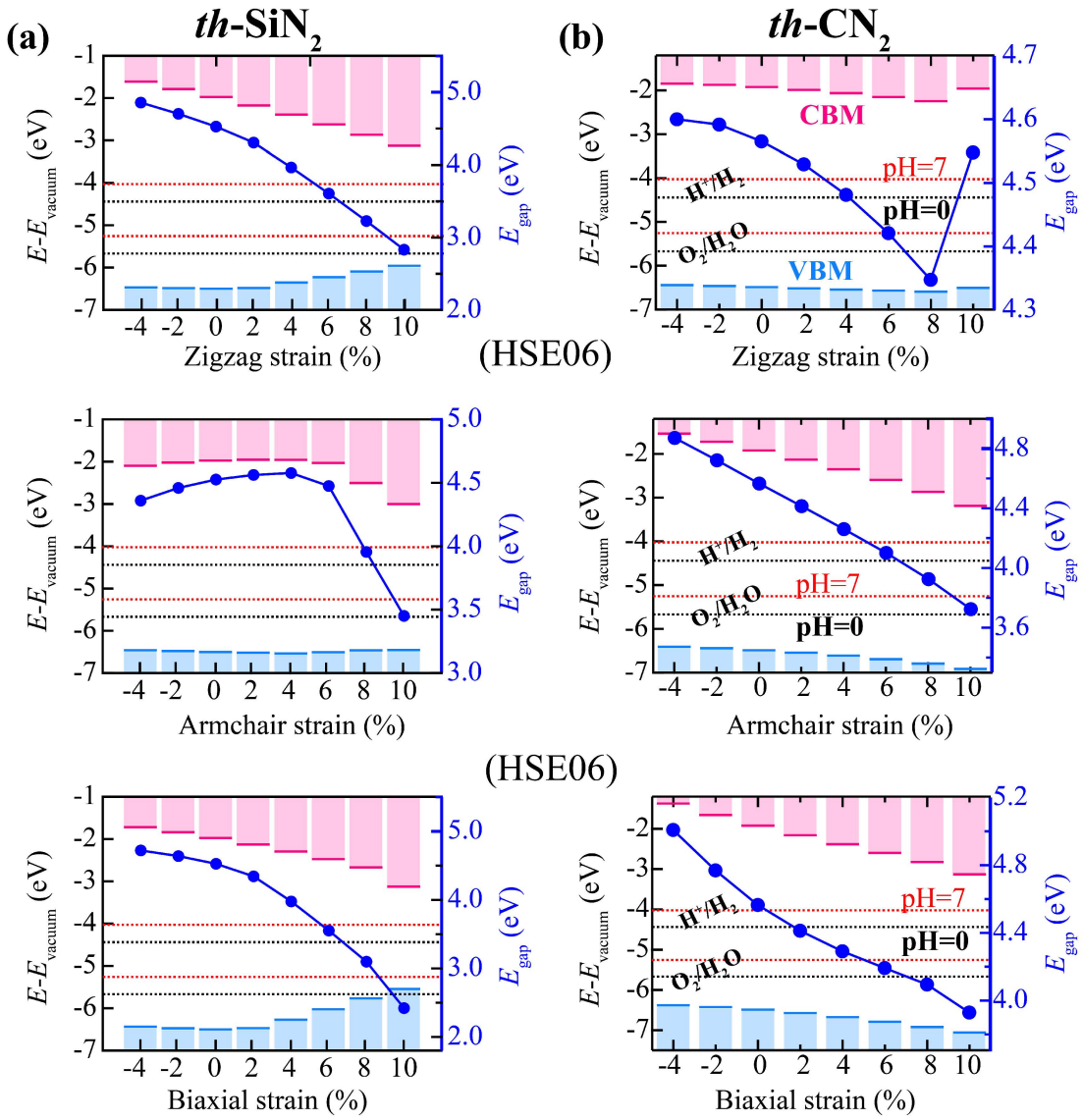

Figure 3.20: Strain engineering of the electronic properties (band gap and band edges alignment with respect to the redox potential of water splitting) of the $th-XN_2$ compounds, calculated from HSE06 functional, for zigzag, armchair, and biaxial strains within the range of -4% to 10% (negative/positive numbers correspond to the compressive/tensile strain), with increments of 2%. The dark blue markers depict the band gap values. The valence band maximum (VBM) and conduction band minimum (CBM) positions are shown with purple and blue bars, respectively. The redox potentials of water splitting are accentuated by red and black dashed lines for pH=7 and pH=0, respectively.

the band gap energy of the crystal should be sufficiently low to provide a proper absorption in the visible region of the light spectrum which covers around 43% of the solar incident beams. Therefore, a tensile strain can be employed to increase the light absorption efficiency of the *th*-XN_2 compounds.

3.3.6 Effective mass and carrier mobility

The effective mass and carrier mobility of the *th*-XN_2 compounds were studied to achieve a better insight into the migration characteristics of the charge carriers. The effective mass was calculated, using Eq. 3.9. We found that in the *th*-XN_2 compounds, the effective mass is highly direction-dependent. The calculated values of effective mass along the zigzag (x) and armchair (y) directions are reported in Table 3.7. In the case of *th*-SiN_2, the effective mass of electrons along the zigzag direction is 22 times higher than the armchair direction. In contrast, the effective mass of holes is 3.46 times higher along the armchair direction. Moreover, the type of charge carrier has a significant effect on the effective mass; in a way that along the zigzag direction the effective mass of electrons is 46 times higher than that of holes. The charge carriers of *th*-CN_2 also exhibit a similar direction and type-dependent effective mass. To visualize the scope of this anisotropy, we presented the angle dependence of the electron and hole effective masses of *th*-SiN_2 in Fig. 3.21 (a). It can be seen that electrons and holes have their maximum effective mass along the armchair and zigzag directions, respectively. In the next step, we investigated the charge carrier mobilities along the ΓX (denoted by μ_x^{2D}) and ΓY (denoted by μ_y^{2D}) directions through Eq. 3.10. One can see that mobility depends on anisotropic factors, such as effective mass. Consequently, the *th*-XN_2 compounds have highly direction-dependent carrier mobilities (see Table 3.7). Since electrons and holes play a key role in the photocatalysis process, an efficient photocatalyst needs to have a prolonged charge carrier drift time. To achieve this requirement, the photo-generated electron/hole pairs should get separated to prevent quick recombination of them and it is the difference in the mobilities of the electron and hole that induces this separation. Accordingly, the *th*-XN_2 compounds, which offer inequivalent and direction-dependent electron

Table 3.7: Charge carrier properties, where m_x^*/m_0 and m_y^*/m_0 are the effective masses with respect to a static electron mass (m_0) along the zigzag and armchair edges, C_{2D} is the elastic constant in the unit of N/m, E_1 is the deformation potential constant in the unit of eV, and μ^{2D} is the charge carrier mobility in the unit of $cm^2V^{-1}s^{-1}$ at T=300 K.

		Effective mass		In-plane stifness		Deformation pot.		Mobility × 10^3	
Structure	Carrier type	m_x^*/m_0	m_y^*/m_0	C_{2D}^x	C_{2D}^y	E_1^x	E_1^y	μ_x^{2D}	μ_y^{2D}
th-SiN_2	Hole	0.28	0.97	182.20	184.28	9.80	1.57	0.28	3.14
	Electron	13.00	0.59	182.20	184.28	0.59	1.06	0.31	2.13
th-CN_2	Hole	0.44	1.09	338.36	195.27	3.12	10.34	2.42	0.05
	Electron	0.22	0.33	338.36	195.27	1.50	2.62	55.97	6.96

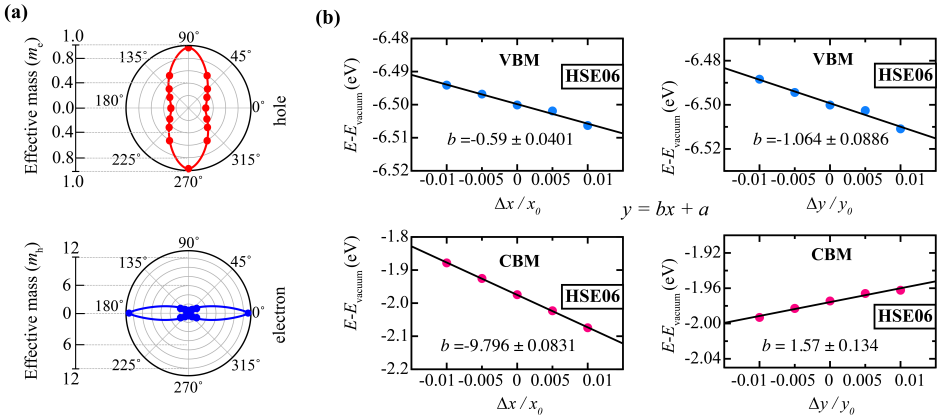

Figure 3.21: (a) The evolution of effective mass *vs* in-plane angle for electrons (top panel) and holes (bottom panel) in *th*−SiN_2. (b) Dependence of total energy (calculated by the HSE06 functional) of band edges (CBM and VBM positions) with respect to the vacuum level as a function of applied uniaxial strains along the transport direction for *th*−SiN_2.

and hole mobilities, are promising candidates for application in photocatalysis processes.

3.3.7 Optical properties

The light-harvesting performance of the *th*-XN_2 compounds was investigated, using GW_0+BSE method. The resulted optical absorption coefficient *vs* the light energy plots are provided in Fig. 3.22, where x and y symbolize simulation along

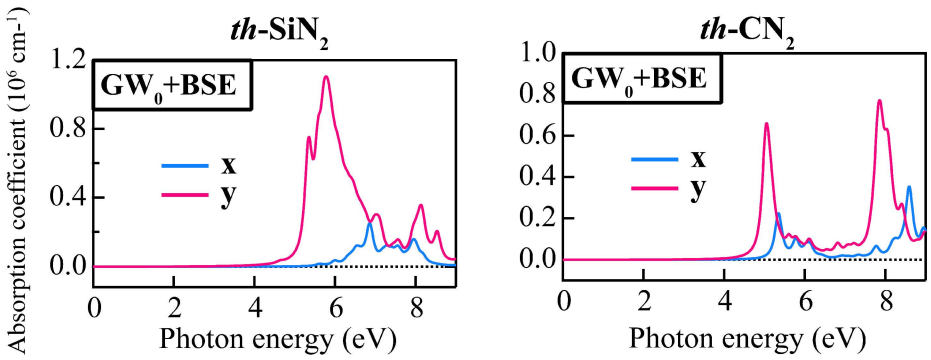

Figure 3.22: The optical absorption coefficient of the $th-XN_2$ compounds along zigzag (x) and armchair (y) edges as a function of photon energy, calculated based on the GW_0+BSE method.

zigzag and armchair edge, respectively. In both compounds, the absorption coefficient is highly direction-dependent, where the absorption strength along the armchair edge outweighs the zigzag edge. This highly anisotropic optical behavior of the *th*-XN_2 compounds stems from their anisotropic charge distribution, and can be exploited to manipulate the polarization of the incident light. In both compounds, a heavy absorption occurs in the ultraviolet region of the light spectrum, where the absorption coefficient is in the order of 10^6 cm^{-1}. In *th*-SiN_2, and along the armchair direction, a great absorption peak appears around 6 eV, and a smaller peak emerges around 8.1 eV. Along the zigzag edge, however, a weak absorption occurs between 6 and 8 eV. In general, similar light absorption behavior can be found in *th*-CN_2. Along the armchair direction, however, peaks are slightly shifted towards lower energies, where two nearly equivalent peaks arise around 5 and 8 eV. In this material, the weak absorption along the zigzag edge is broken into two peaks, one lies near 5.5 eV and the other one appears around 8.6 eV. From an energetic point of view, an ultraviolet beam can facilitate photocatalytic activities better than visible light, since its high photonic energy is enough to overcome large energy barriers in a catalysis process. Therefore, the *th*-XN_2 compounds can be utilized as photocatalysts where a broad energy barrier exists.

Chapter 4

Conclusion

In this last chapter, briefly, we present our conclusions drawn from this thesis. Our first-principles calculations revealed that a plethora of exotic properties can be found in the Tetrahex compounds. In the first step, based on cohesive energy, phonon spectrum, AIMD simulations, and Born-Huang elastic stability criteria, we revealed that these materials are energetically, dynamically, thermally, and mechanically stable, respectively. We found that the intrinsic structural anisotropy of these compounds creates unique direction-dependent mechanical, electronic, and optical properties, such as angle-dependent high Young modulus, negative Poisson's ratio, and excellent ultimate strain comparable to that of graphene, making them suitable for strain engineering of electronic and optical properties. Auxetic materials are rare, and materials with auxetic behavior in their equilibrium state are far more scarce. The appearance of these unconventional properties in the *th*-CN_2 and *th*-SiN_2 compounds makes them promising for numerous applications in industry. Among these compounds, we can find natural semiconductors, with direct, quasi-direct, and indirect band gaps. Moreover, the majority have a band gap that lies perfectly in the suitable region of the solar spectrum for optimum light absorption, which is simultaneously wide enough to provide sufficient photo-generated energy to overcome the potential barrier of water splitting. They also have highly anisotropic charge carrier mobility, which provides a suitable condition for exciton separation, and prolongs

the average lifetime of electron-hole pairs. Among these 2D materials, in pristine condition, *th*-CP_2 and *th*-CAs_2 have the proper band alignment with the oxidation/reduction potential of water splitting. Moreover, this alignment can be improved in *th*-CAs_2 through strain manipulation of the electronic properties. Thus, these compounds can be considered as suitable candidates for high-performance photo-induced catalysis of the water-splitting process. Finally, due to the versatility of the sp^3 orbital hybridization found in the Tetrahex compounds, we predict that other binary and ternary compounds from the block p of the periodic table can be materialized in this skeleton, each of which can probably possess a plethora of exotic properties. Thus, fruitful studies can be conducted on this family of 2D materials in the recent future.

Bibliography

[1] K. S. Novoselov, A. K. Geim, S. V. Morozov, D. Jiang, Y. Zhang, S. V. Dubonos, I. V. Grigorieva, and A. A. Firsov, "Electric field effect in atomically thin carbon films," *science*, vol. 306, no. 5696, pp. 666–669, 2004.

[2] K. S. Novoselov, A. K. Geim, S. V. Morozov, D. Jiang, M. I. Katsnelson, I. Grigorieva, S. Dubonos, and A. Firsov, "Two-dimensional gas of massless dirac fermions in graphene," *nature*, vol. 438, no. 7065, pp. 197–200, 2005.

[3] Y. Zhang, Y.-W. Tan, H. L. Stormer, and P. Kim, "Experimental observation of the quantum hall effect and berry's phase in graphene," *nature*, vol. 438, no. 7065, pp. 201–204, 2005.

[4] A. K. Geim and K. S. Novoselov, *The rise of graphene*. World Scientific, 2010.

[5] P. R. Wallace, "The band theory of graphite," *Phys. Rev.*, vol. 71, no. 9, p. 622, 1947.

[6] F. Schwierz, "Graphene transistors," *Nat. Nanotechnol.*, vol. 5, no. 7, p. 487, 2010.

[7] X. Li, J. Yu, S. Wageh, A. A. Al-Ghamdi, and J. Xie, "Graphene in photocatalysis: a review," *Small*, vol. 12, no. 48, pp. 6640–6696, 2016.

[8] M. E. Kilic and K.-R. Lee, "Tuning the electronic, mechanical, thermal, and optical properties of tetrahexcarbon via hydrogenation," *Carbon*, vol. 161, pp. 71–82, 2020.

[9] S. Zhang, J. Zhou, Q. Wang, X. Chen, Y. Kawazoe, and P. Jena, "Penta-graphene: A new carbon allotrope," *PNAS*, vol. 112, no. 8, pp. 2372–2377, 2015.

[10] B. Ram and H. Mizuseki, "Tetrahexcarbon: A two-dimensional allotrope of carbon," *Carbon*, vol. 137, pp. 266–273, 2018.

[11] H. Sun, S. Mukherjee, and C. V. Singh, "Mechanical properties of monolayer penta-graphene and phagraphene: a first-principles study," *Phys. Chem. Chem. Phys.*, vol. 18, no. 38, pp. 26736–26742, 2016.

[12] J. Kotakoski, J. C. Meyer, S. Kurasch, D. Santos-Cottin, U. Kaiser, and A. V. Krasheninnikov, "Stone-wales-type transformations in carbon nanostructures driven by electron irradiation," *Phys. Rev. B*, vol. 83, no. 24, p. 245420, 2011.

[13] C. Wang and Y.-h. Ding, "Catalytically healing the stone–wales defects in graphene by carbon adatoms," *J. Mater. Chem. A*, vol. 1, no. 5, pp. 1885–1891, 2013.

[14] F. M. de Vasconcelos, A. G. Souza Filho, V. Meunier, and E. C. Girão, "Electronic properties of tetragraphene nanoribbons," *Phys. Rev. Mater.*, vol. 3, no. 6, p. 066002, 2019.

[15] F. M. de Vasconcelos, A. G. Souza Filho, V. Meunier, and E. C. Girão, "Electronic and structural properties of tetragraphenes," *Carbon*, vol. 167, pp. 403–413, 2020.

[16] M. E. Kilic and K.-R. Lee, "Tetrahex carbides: Two-dimensional group-iv materials for nanoelectronics and photocatalytic water splitting," *Carbon*, vol. 174, pp. 368–381, 2021.

[17] S. Zhang, J. Zhou, Q. Wang, and P. Jena, "Beyond graphitic carbon nitride: nitrogen-rich penta-CN2 sheet," *J. Phys. Chem. C*, vol. 120, no. 7, pp. 3993–3998, 2016.

[18] S. Sun, F. Meng, Y. Xu, J. He, Y. Ni, and H. Wang, "Flexible, auxetic and strain-tunable two dimensional penta-X2C family as water splitting photocatalysts with high carrier mobility," *J. Mater. Chem. A*, vol. 7, no. 13, pp. 7791–7799, 2019.

[19] M. Abutalib, "A new antimony carbide monolayer: An indirect semiconductor with a tunable band gap," *Chem. Phys. Lett.*, vol. 708, pp. 188–193, 2018.

[20] S. Cahangirov, H. Sahin, G. Le Lay, and A. Rubio, *Introduction to the Physics of Silicene and other 2D Materials*, vol. 930. Springer, 2016.

[21] S. Das, J. A. Robinson, M. Dubey, H. Terrones, and M. Terrones, "Beyond graphene: progress in novel two-dimensional materials and van der waals solids," *Annu. Rev. Mater. Res.*, vol. 45, pp. 1–27, 2015.

[22] Z. Guo, J. Zhou, L. Zhu, and Z. Sun, "Mxene: a promising photocatalyst for water splitting," *J. Mater. Chem. A*, vol. 4, no. 29, pp. 11446–11452, 2016.

[23] A. K. Singh, K. Mathew, H. L. Zhuang, and R. G. Hennig, "Computational screening of 2d materials for photocatalysis," *J. Phys. Chem. Lett.*, vol. 6, no. 6, pp. 1087–1098, 2015.

[24] B. Luo, G. Liu, and L. Wang, "Recent advances in 2d materials for photocatalysis," *Nanoscale*, vol. 8, no. 13, pp. 6904–6920, 2016.

[25] Y. Sun, H. Cheng, S. Gao, Z. Sun, Q. Liu, Q. Liu, F. Lei, T. Yao, J. He, S. Wei, *et al.*, "Freestanding tin disulfide single-layers realizing efficient visible-light water splitting," *Angew. Chem. Int. Ed.*, vol. 51, no. 35, pp. 8727–8731, 2012.

[26] Y. Sun, Z. Sun, S. Gao, H. Cheng, Q. Liu, J. Piao, T. Yao, C. Wu, S. Hu, S. Wei, *et al.*, "Fabrication of flexible and freestanding zinc chalcogenide single layers," *Nat. Commun.*, vol. 3, no. 1, pp. 1–7, 2012.

[27] D. Voiry, H. Yamaguchi, J. Li, R. Silva, D. C. Alves, T. Fujita, M. Chen, T. Asefa, V. B. Shenoy, G. Eda, *et al.*, "Enhanced catalytic activity in

strained chemically exfoliated WS2 nanosheets for hydrogen evolution," *Nat. Mater.*, vol. 12, no. 9, pp. 850–855, 2013.

[28] Y. Xu, W. Zhao, R. Xu, Y. Shi, and B. Zhang, "Synthesis of ultrathin cds nanosheets as efficient visible-light-driven water splitting photocatalysts for hydrogen evolution," *Chem. Commun.*, vol. 49, no. 84, pp. 9803–9805, 2013.

[29] R. Peng, Y. Ma, Q. Wu, B. Huang, and Y. Dai, "Two-dimensional materials with intrinsic auxeticity: progress and perspectives," *Nanoscale*, vol. 11, no. 24, pp. 11413–11428, 2019.

[30] P. Mardling, A. Alderson, N. Jordan-Mahy, and C. L. Le Maitre, "The use of auxetic materials in tissue engineering," *Biomater. Sci.*, vol. 8, no. 8, pp. 2074–2083, 2020.

[31] R. S. Underhill, "Dsiac journal• volume 1• no. 1• july 2014/7,"

[32] Y. Liu and H. Hu, "A review on auxetic structures and polymeric materials," *Sci. Res. Essays*, vol. 5, no. 10, pp. 1052–1063, 2010.

[33] C. Huang and L. Chen, "Negative poisson's ratio in modern functional materials," *Adv. Mater.*, vol. 28, no. 37, pp. 8079–8096, 2016.

[34] E. Schrödinger, "An undulatory theory of the mechanics of atoms and molecules," *Phys. Rev.*, vol. 28, no. 6, p. 1049, 1926.

[35] D. R. Hartree, "The wave mechanics of an atom with a non-coulomb central field. part i. theory and methods," in *Mathematical Proceedings of the Cambridge Philosophical Society*, vol. 24, pp. 89–110, Cambridge university press, 1928.

[36] J. C. Slater, "Note on hartree's method," *Phys. Rev.*, vol. 35, no. 2, p. 210, 1930.

[37] V. Fock, "N "a method for solving the quantum mechanical multiple ö rper problem," *J. Phys.*, vol. 61, no. 1-2, pp. 126–148, 1930.

[38] L. H. Thomas, "The calculation of atomic fields," in *Mathematical proceedings of the Cambridge philosophical society*, vol. 23, pp. 542–548, Cambridge University Press, 1927.

[39] E. Fermi, "A statistical method for determining some properties of the atom and its application to the theory of the periodic table of elements," *J. Phys.*, vol. 48, no. 1-2, pp. 73–79, 1928.

[40] P. Hohenberg and W. Kohn, "Inhomogeneous electron gas," *Phys. Rev.*, vol. 136, no. 3B, p. B864, 1964.

[41] W. Kohn and L. J. Sham, "Self-consistent equations including exchange and correlation effects," *Phys. Rev.*, vol. 140, no. 4A, p. A1133, 1965.

[42] R. O. Jones and O. Gunnarsson, "The density functional formalism, its applications and prospects," *Rev. Mod. Phys.*, vol. 61, no. 3, p. 689, 1989.

[43] J. P. Perdew and Y. Wang, "Accurate and simple analytic representation of the electron-gas correlation energy," *Phys. Rev. B*, vol. 45, no. 23, p. 13244, 1992.

[44] P. E. Blöchl, "Projector augmented-wave method," *Phys. Rev. B*, vol. 50, no. 24, p. 17953, 1994.

[45] G. Kresse and D. Joubert, "From ultrasoft pseudopotentials to the projector augmented-wave method," *Phys. Rev. B*, vol. 59, no. 3, p. 1758, 1999.

[46] G. Kresse and J. Hafner, "Norm-conserving and ultrasoft pseudopotentials for first-row and transition elements," *J. Phys. Condens. Matter*, vol. 6, no. 40, p. 8245, 1994.

[47] J. P. Perdew, K. Burke, and M. Ernzerhof, "Generalized gradient approximation made simple," *Phys. Rev. Lett.*, vol. 77, no. 18, p. 3865, 1996.

[48] H. J. Monkhorst and J. D. Pack, "Special points for brillouin-zone integrations," *Phys. Rev. B*, vol. 13, no. 12, p. 5188, 1976.

[49] J. Heyd, G. E. Scuseria, and M. Ernzerhof, "Hybrid functionals based on a screened coulomb potential," *J. Chem. Phys.*, vol. 118, no. 18, pp. 8207–8215, 2003.

[50] J. Paier, M. Marsman, K. Hummer, G. Kresse, I. C. Gerber, and J. G. Ángyán, "Screened hybrid density functionals applied to solids," *J. Chem. Phys.*, vol. 124, no. 15, p. 154709, 2006.

[51] L. Chaput, A. Togo, I. Tanaka, and G. Hug, "Phonon-phonon interactions in transition metals," *Phys. Rev. B*, vol. 84, no. 9, p. 094302, 2011.

[52] S. Nosé, "A unified formulation of the constant temperature molecular dynamics methods," *J. Chem. Phys.*, vol. 81, no. 1, pp. 511–519, 1984.

[53] S. Nosé, "A molecular dynamics method for simulations in the canonical ensemble," *Mol. Phys.*, vol. 52, no. 2, pp. 255–268, 1984.

[54] W. G. Hoover, "Canonical dynamics: Equilibrium phase-space distributions," *Phys. Rev. A*, vol. 31, no. 3, p. 1695, 1985.

[55] G. Onida, L. Reining, and A. Rubio, "Electronic excitations: density-functional versus many-body green's-function approaches," *Rev. Mod. Phys.*, vol. 74, no. 2, p. 601, 2002.

[56] S. Albrecht, L. Reining, R. Del Sole, and G. Onida, "Ab initio calculation of excitonic effects in the optical spectra of semiconductors," *Phys. Rev. Lett.*, vol. 80, no. 20, p. 4510, 1998.

[57] M. Rohlfing and S. G. Louie, "Electron-hole excitations in semiconductors and insulators," *Phys. Rev. Lett.*, vol. 81, no. 11, p. 2312, 1998.

[58] T. L. Cottrell, *The strengths of chemical bonds*. Butterworths Scientific Publications, 1958.

[59] N. Drummond, V. Zolyomi, and V. Fal'Ko, "Electrically tunable band gap in silicene," *Phys. Rev. B*, vol. 85, no. 7, p. 075423, 2012.

[60] S. Cahangirov, M. Topsakal, E. Aktürk, H. Şahin, and S. Ciraci, "Two- and one-dimensional honeycomb structures of silicon and germanium," *Phys. Rev. Lett.*, vol. 102, no. 23, p. 236804, 2009.

[61] V. Vierimaa, A. V. Krasheninnikov, and H.-P. Komsa, "Phosphorene under electron beam: from monolayer to one-dimensional chains," *Nanoscale*, vol. 8, no. 15, pp. 7949–7957, 2016.

[62] M. Born and K. Huang, *Dynamical theory of crystal lattices*. Clarendon press, 1954.

[63] C. Lee, X. Wei, J. W. Kysar, and J. Hone, "Measurement of the elastic properties and intrinsic strength of monolayer graphene," *science*, vol. 321, no. 5887, pp. 385–388, 2008.

[64] R. Lakes, "Response: negative poisson's ratio materials," *Science*, vol. 238, no. 4826, pp. 551–551, 1987.

[65] G. N. Greaves, A. Greer, R. S. Lakes, and T. Rouxel, "Poisson's ratio and modern materials," *Nat. Mater.*, vol. 10, no. 11, pp. 823–837, 2011.

[66] Q. Liu, *Literature review: materials with negative Poisson's ratios and potential applications to aerospace and defence*. Defence Science and Technology Organisation Victoria (Australia) Air ..., 2006.

[67] Q. Wei, Y. Yang, A. Gavrilov, and X. Peng, "A new 2d auxetic CN2 nanostructure with high energy density and mechanical strength," *Phys. Chem. Chem. Phys.*, vol. 23, no. 7, pp. 4353–4364, 2021.

[68] F. Liu, P. Ming, and J. Li, "Ab initio calculation of ideal strength and phonon instability of graphene under tension," *Phys. Rev. B*, vol. 76, no. 6, p. 064120, 2007.

[69] A. Rawat, N. Jena, A. De Sarkar, *et al.*, "A comprehensive study on carrier mobility and artificial photosynthetic properties in group vi b transition metal dichalcogenide monolayers," *J. Mater. Chem. A*, vol. 6, no. 18, pp. 8693–8704, 2018.

[70] H. Lang, S. Zhang, and Z. Liu, "Mobility anisotropy of two-dimensional semiconductors," *Phys. Rev. B*, vol. 94, no. 23, p. 235306, 2016.

[71] M. E. Kilic and K.-R. Lee, "First-principles study of fluorinated tetrahexcarbon: stable configurations, thermal, mechanical, and electronic properties," *J. Phys. Chem. C*, vol. 124, no. 15, pp. 8225–8235, 2020.

[72] H. Eidsvåg, S. Bentouba, P. Vajeeston, S. Yohi, and D. Velauthapillai, "TiO2 as a photocatalyst for water splitting—an experimental and theoretical review," *Molecules*, vol. 26, no. 6, p. 1687, 2021.

[73] H. Liu, G. Qin, Y. Lin, and M. Hu, "Disparate strain dependent thermal conductivity of two-dimensional penta-structures," *Nano Lett.*, vol. 16, no. 6, pp. 3831–3842, 2016.

[74] T. L. Cottrell, *The strengths of chemical bonds*. Butterworths Scientific Publications, 1958.

[75] J.-W. Jiang and H. S. Park, "Negative poisson's ratio in single-layer black phosphorus," *Nat. Commun.*, vol. 5, no. 1, pp. 1–7, 2014.

[76] A. J. Mannix, X.-F. Zhou, B. Kiraly, J. D. Wood, D. Alducin, B. D. Myers, X. Liu, B. L. Fisher, U. Santiago, J. R. Guest, *et al.*, "Synthesis of borophenes: Anisotropic, two-dimensional boron polymorphs," *Science*, vol. 350, no. 6267, pp. 1513–1516, 2015.

[77] M. Yagmurcukardes, H. Sahin, J. Kang, E. Torun, F. M. Peeters, and R. T. Senger, "Pentagonal monolayer crystals of carbon, boron nitride, and silver azide," *J. Appl. Phys.*, vol. 118, no. 10, p. 104303, 2015.

Appendix A

Supplement Materials

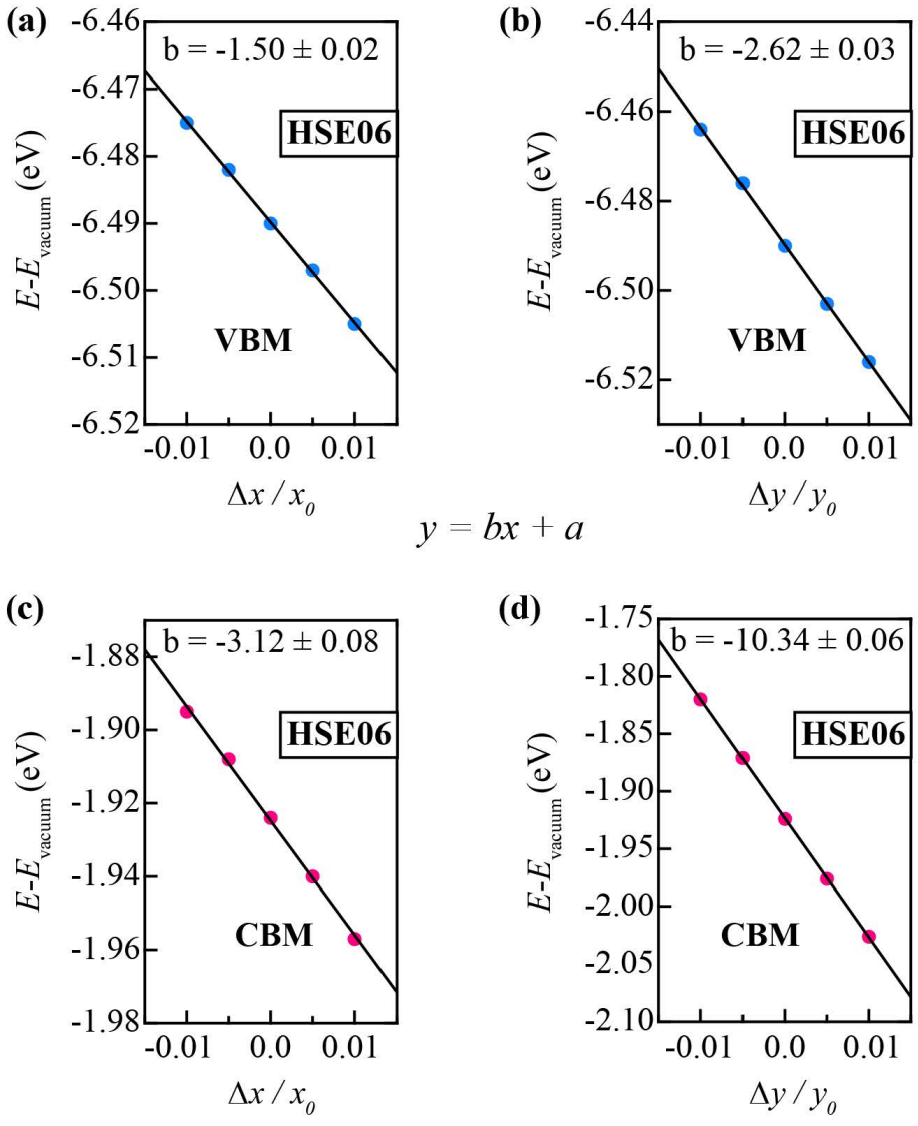

Figure A.1: Dependence of total energy (calculated by the HSE06 functional) of band edges (CBM and VBM positions) versus the vacuum level as a function of applied uniaxial strains along the transport direction for *th*-CN_2. (a) VBM along the zigzag direction. (b) VBM along the armchair direction. (c) CBM along the zigzag direction. and (d) CBM along the armchair direction.

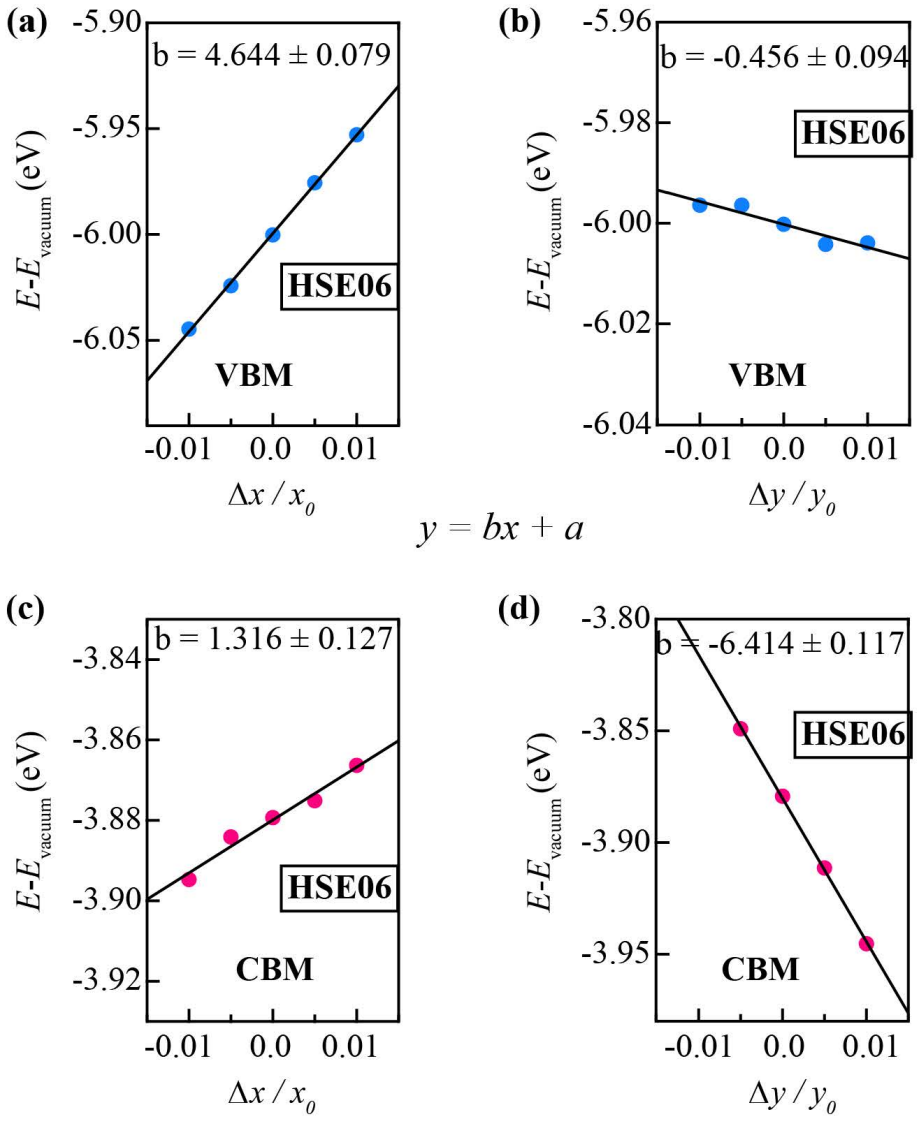

Figure A.2: Dependence of total energy (calculated by the HSE06 functional) of band edges (CBM and VBM positions) versus the vacuum level as a function of applied uniaxial strains along the transport direction for *th*-CP_2. (a) VBM along the zigzag direction. (b) VBM along the armchair direction. (c) CBM along the zigzag direction. and (d) CBM along the armchair direction.

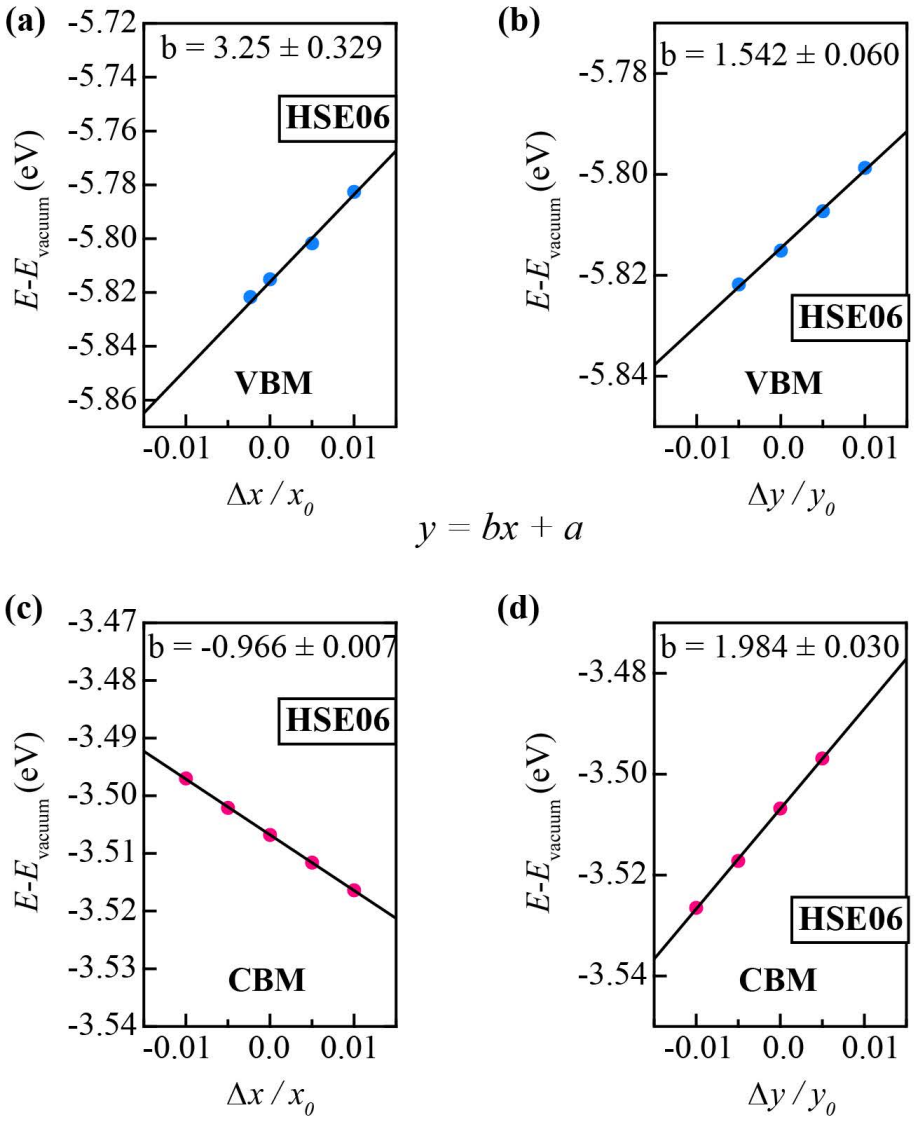

Figure A.3: Dependence of total energy (calculated by the HSE06 functional) of band edges (CBM and VBM positions) versus the vacuum level as a function of applied uniaxial strains along the transport direction for *th*-CAs_2. (a) VBM along the zigzag direction. (b) VBM along the armchair direction. (c) CBM along the zigzag direction. and (d) CBM along the armchair direction.

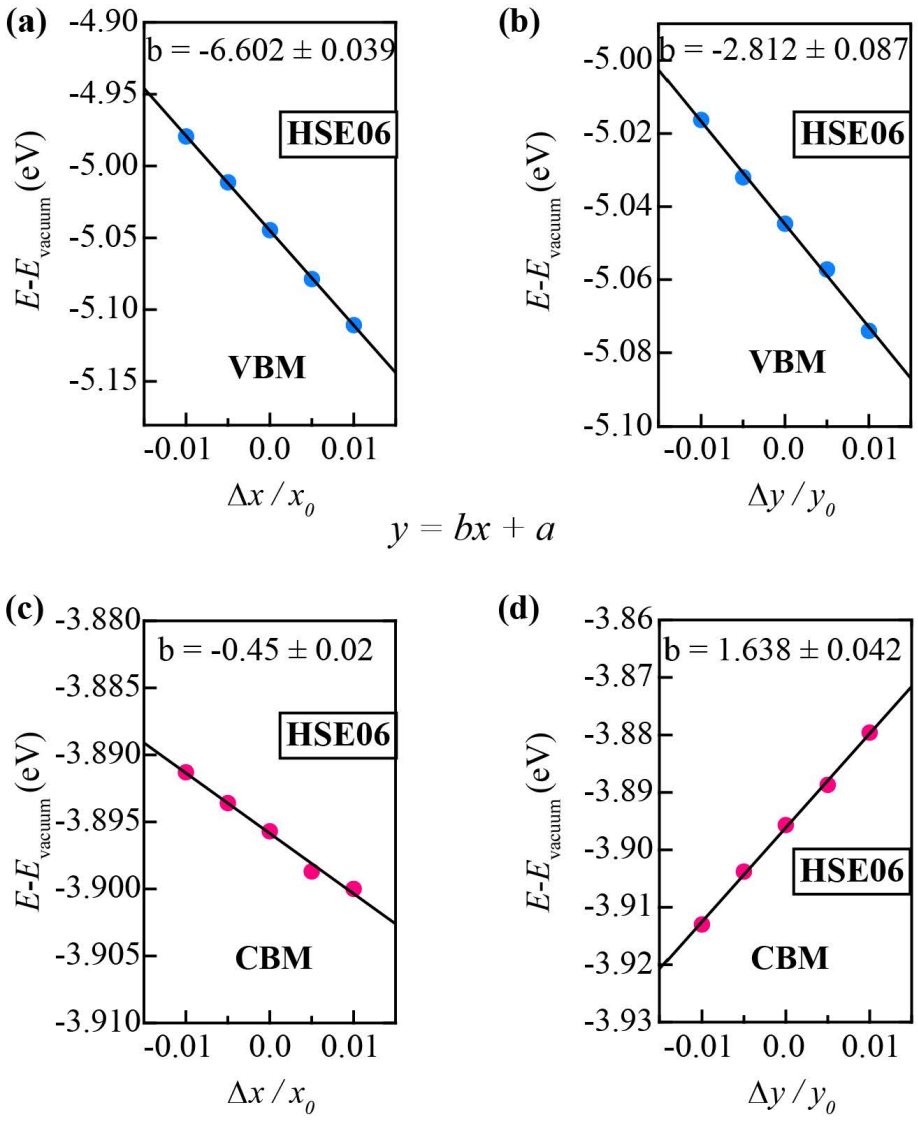

Figure A.4: Dependence of total energy (calculated by the HSE06 functional) of band edges (CBM and VBM positions) versus the vacuum level as a function of applied uniaxial strains along the transport direction for *th*-CSb_2. (a) VBM along the zigzag direction. (b) VBM along the armchair direction. (c) CBM along the zigzag direction. and (d) CBM along the armchair direction.

POSCAR of relaxed structure of *th*-CN_2:

th-CN2

1.00000000000000

4.1771564257899998 0.0000000000000000 0.0000000000000000

0.0000000000000000 5.7817761805099996 0.0000000000000000

0.0000000000000000 0.0000000000000000 20.0000000000000000

C N

4 8

Direct

0.0000000000000000 0.2500000000000000 0.4999999806327082

0.0000000000000000 0.7499999220000007 0.4999999806327082

0.5000000000000000 0.7499999220000007 0.4999999806327082

0.5000000000000000 0.2500000000000000 0.4999999806327082

0.7499999650000007 0.6266447485786273 0.4654842730274709

0.7499999650000007 0.3733552774213749 0.4654842730274709

0.2500000000000000 0.1266447485786273 0.4654842730274709

0.2500000000000000 0.8733553034213770 0.4654842730274709

0.2500000000000000 0.3733552774213749 0.5345157269725291

0.2500000000000000 0.6266447485786273 0.5345157269725291

0.7499999650000007 0.8733553034213770 0.5345157269725291

0.7499999650000007 0.1266447485786273 0.5345157269725291